GANSim-3D for conditional geomodelling: theory and field application

Suihong Song[1,2], Tapan Mukerji[3], Jiagen Hou[1,4,*], Dongxiao Zhang[5], and Xinrui Lyu[6]

[1] College of Geoscience, China University of Petroleum (Beijing), Beijing, 102249, China.

[2] Intelligent Energy Laboratory, Frontier Research Center, Peng Cheng Laboratory, Shenzhen 518000, China.

[3] Stanford University, 367 Panama St, Stanford, CA 94305, USA.

[4] State Key Laboratory of Petroleum Resources and Prospecting, China University of Petroleum (Beijing), Beijing, 102249, China.

[5] School of Environmental Science and Engineering, Southern University of Science and Technology, Shenzhen 518055, China

[6] Petroleum Exploration and Production Research Institute, Sinopec, Beijing 10083, China

It is non-peer reviewed preprint submitted to Water Resources Research

Contact: Suihong Song (songsuihong@126.com)

Abstract

Geomodelling of subsurface reservoirs is important for water resources, hydrocarbon exploitation, and Carbon Capture and Storage (CCS). Traditional geostatistics-based approaches cannot abstract complex geological patterns and are thus not able to simulate very realistic earth models. We present a Generative Adversarial Networks (GANs)-based 3D reservoir simulation framework, GANSim-3D, which can capture geological patterns and relationships between various conditioning data and earth models and is thus able to directly simulate multiple 3D realistic and conditional earth models of arbitrary sizes from given conditioning data. In GANSim-3D, the generator, designed to only include 3D convolutional layers, takes various 3D conditioning data and 3D random latent cubes (composed of random numbers) as inputs and produces a 3D earth model. Two types of losses, the original GANs loss and condition-based loss, are designed to train the generator progressively from shallow to deep layers to learn the geological patterns and relationships from coarse to fine resolutions. Conditioning data can include 3D sparse well facies data, 3D low-resolution probability maps, and global features like facies proportion, channel width, etc. Once trained on a training dataset where each training sample is a 3D cube of a small fixed size, the generator can be used for geomodelling of 3D reservoirs of large arbitrary sizes by directly extending the sizes of all inputs and the output of the generator proportionally. To illustrate how GANSim-3D is used for field geomodelling and also to verify GANSim-3D, a field karst cave reservoir in Tahe area of China is used as an example. The 3D well facies data and 3D probability map of caves obtained from geophysical interpretation are used as conditioning data. First, we create a training dataset consisting of facies models of 64×64×64 cells with a process-mimicking simulation method to integrate field geological patterns. The training well facies data and the training probability map data are produced from the training facies models. Then, the 3D generator is successfully trained and evaluated in two synthetic cases with various metrics. Next, we apply the pretrained generator for conditional geomodelling of two field cave reservoirs of Tahe area. The first reservoir is 800m × 800m × 64m and is divided into 64 × 64 × 64 cells, while the second is 4200m×3200m×96m and is divided into 336×256×96 cells. We fix the input well facies data and cave probability maps and randomly change the input latent cubes to allow the generator to produce multiple diverse cave reservoir realizations, which prove to be consistent with the geological patterns of real Tahe cave reservoir as well as the input conditioning data. The noise in the input probability map is suppressed by the generator. Once trained, the geomodelling process is quite fast: each realization with 336×256×96 cells takes 0.988 seconds using 1 GPU (V100). This study shows that GANSim-3D is robust for fast 3D conditional geomodelling of field reservoirs of arbitrary sizes.

Key Points:

- GANSim-3D produces multiple 3D realistic conditional reservoir models of arbitrary sizes from given conditioning data.
- Application in field karst cave reservoirs shows robust performance of GANSim-3D.
- Geomodelling with GANSim-3D is quite fast: <1s for one realization with 336×256×96 cells.

1 Introduction

Geomodelling, or quantitatively predicting the distribution of subsurface reservoirs, is of great significance for evaluation and exploitation of underground water and energy resources as well as for geological sequestration of CO_2 (CCS). Generally, various types of information (data) about the subsurface are incorporated using geostatistical approaches for geomodelling. Such information includes sparse well data, geophysical data, global features (e.g., facies proportion), and spatial geological patterns, among which the geological patterns may be the most difficult to incorporate. In traditional geostatistics-based geomodelling approaches, geological patterns can be partially expressed by simple variogram functions (e.g., in Sequential Indicator Simulation method; Pyrcz & Deutsch, 2014) or local multiple points statistics (MPS) (in MPS-based approaches; Mariethoz & Caers, 2014). Such partial representations may not be able to completely express the complicated spatial geological patterns, thus there is a lack of realism (expected geological patterns) to different extents in the simulated results of these approaches, e.g., facies models produced by variogram-based approaches cannot exhibit sinuous channel-like shapes, while MPS-based approaches may produce discontinuous channels. In addition, due to the incompleteness and imperfectness of the incorporated information (e.g., the sparse nature of well data and low-resolution nature of geophysical data), uncertainty exists in geomodelling results, so a number of reservoir realizations are generally produced to represent the potential distribution of subsurface reservoirs.

Generative Adversarial Networks (GANs) (Goodfellow et al., 2014) in deep learning are good at capturing complete spatial patterns (structures) of 2D images or 3D objects using a generator Convolutional Neural Network (CNN), with the help of another discriminator CNN. With the captured pattern knowledge, the generator CNN can map a random latent vector into a realistic image or a realistic 3D object (e.g., Wu et al., 2016). Supporting Information S1 gives more detail about the basic methodology of GANs.

In recent years, GANs have been combined with geomodelling on different aspects (e.g., Chan & Elsheikh, 2017, 2019; Dupont et al., 2018; Laloy et al., 2018; Mosser et al., 2020; Zheng & Zhang, 2022; Nesvold & Mukerji, 2021; Song et al., 2021a, 2021b, 2022; Zhang et al., 2019). Like any other approach, unconditional and conditional geomodelling are considered. For unconditional GANs-based geomodelling, the generator CNN is first trained to abstract spatial geological patterns from training facies models; then it uses the learned pattern knowledge to quickly produce multiple reservoir realizations consistent with the pattern from random latent vectors. Song et al. (2021a) proposed to use a progressive training approach for GANs in geomodelling, going incrementally from coarse resolution to finer and finer resolutions and proved that it performs better than the conventional alternative of training where the finest resolution is directly produced.

There are two approaches to achieve conditioning in GANs-based geomodelling. Note that the trained generator in the unconditional case can map a random latent vector into any realistic facies model, so the key of the first conditioning approach is to search for appropriate input latent vectors, with which the trained generator can produce facies models consistent with expected geological patterns as well as given conditioning data. Laloy et al. (2018), Mosser et al. (2020), and Nesvold & Mukerji (2021) used Markov Chain Monte Carlo optimization algorithms (MCMC) to search for such appropriate latent vectors, while Dupont et al. (2018) and Zhang et al. (2019) used gradient descent optimization algorithms. With these optimization-based algorithms, only one optimal latent vector is found every time, and thus many optimization runs are needed to produce multiple latent vectors and their corresponding multiple facies models for uncertainty assessment. Chan & Elsheikh (2019) proposed to train an extra neural network between a predefined distribution (e.g., Gaussian distribution) and all appropriate latent vectors for given conditioning data. In this way, multiple conditional facies models can be obtained all at once. However, the extra neural network is unique for the given conditioning data, and once the conditioning data changes the neural network has to be trained again.

Song et al. (2021b, 2022) proposed another direct conditioning approach, called GANSim, where the generator directly takes conditioning data and random latent vectors as inputs to produce multiple conditional earth models of reservoir. The proposal of GANSim is inspired by the process of experts drawing conditional geological maps by hand, where experts use the geological pattern knowledge and relationship knowledge between conditioning data and geological maps to finish realistic maps consistent with both expected patterns and given conditioning data. The trained generator in the unconditional case only learns the pattern knowledge; in GANSim, a condition-based loss function is further introduced to force the generator also to learn the relationships between various conditioning data and earth models. These conditioning data can include global features (e.g., facies proportion, channel sinuosity, and channel width), local well facies interpretations, and probability maps of geobodies produced from geophysical interpretations. With the learned geological pattern knowledge and the relationship, the trained generator can directly map observed conditioning data into multiple realistic conditional earth models. Compared to the previous approach, GANSim does not involve optimization or extra neural network training process, and thus is more convenient and faster.

However, there are still several aspects that need to be further improved in the current GANSim research presented by Song et al. (2021b, 2022). First, the current GANSim algorithm is presented in a 2D framework, where the input well data, input probability map, and the output reservoir models are all set as 2D (i.e., planner sections of real 3D reservoir) and the CNNs of generator and discriminator also use 2D convolutional kernels. But real subsurface reservoirs are 3D. How to extend GANSim into 3D space? Second, in the current GANSim framework, the trained generator can only produce earth models with a fixed size equal to that on which it was originally trained, e.g, if the training facies models have 64×64 cells each representing 10m×10m, then the trained generator also produces facies models of 64×64 cells. However, the field reservoir to be predicted may be at large arbitrary sizes, different from the size of the training models. Is it possible to use the generator trained on small-size facies models for geomodelling of field reservoirs of large sizes? Third, Song et al. (2021b, 2022) only use synthetic cases to validate the proposed GANSim. Given much more sophisticated geological patterns of field reservoirs than synthetic patterns, field reservoirs are needed to verify the effectiveness and efficiency of GANSim.

Therefore, in this study, we propose a GANSim-3D framework to address the aforementioned concerns based on the GANSim research presented by Song et al. (2021b, 2022). In GANSim-3D, the convolutional kernels of the generator and discriminator, the input conditioning data, and the output earth models are all designed to be 3D, and the architecture design of the generator is specially improved so that it can produce earth models of flexible sizes after being trained on samples of small fixed size. A 3D field karst cave reservoir in Tahe area of China, which proved to be very difficult for geomodelling after many years' research (Liu et al., 2012; Lu et al., 2012; Li et al., 2016(a); Li et al., 2016(b)), is taken as an example to validate the proposed GANSim-3D framework and showcase the field application of GANSim-3D.

Tahe area is located at Akekule uplift of northern Tarim Basin in western China and has an area of around 60km×30km. The major reservoir is Ordovician carbonate karst caves about 5500 meters beneath the surface, including connected ribbon-like caves formed by paleo-underground rivers, isolated caves formed by intermittent surficial water, and fault-controlled caves controlled by strike slip faults and related dissolutions (Lu et al., 2020). These caves were formed when the Ordovician carbonate rock with extensive faults and fractures produced in earlier geomechanical stages was exposed to weathering during the middle Caledonian and Hercynian periods. The Ordovician carbonate rock may experience multiple episodes of weathering in some parts, where in each episode the carbonate rock is uplifted, exposed to weathering, and then subsided, producing multiple layers of caves that are vertically stacked. The unconformity surface (of the last weathering episode) under which the caves are formed is designated as the paleo-geographic surface in this paper. In addition to the vertical multi-layer feature, Tahe caves also have a very strong heterogeneity and complicated spatial patterns in planar view. The diameter of the caves spans from tens of centimeters to tens of meters. Caves tend to develop in the vicinity of different levels of faults, especially where multiple faults intersect. There are three extension directions for the underground river caves: NNE, NNW, and nearly EW. Sparsely distributed hall caves with size several times larger than normal caves and cave branches with different length randomly develop in the underground river cave systems. Section 3 shows more detail about the spatial structure of the underground river cave systems.

These caves can be fully or partially filled by clastic or chemical cement, or totally void without any fill. Compared to the surrounding tight carbonate rock with porosity of less than 1%, these caves, even when completely filled (porosity can be >20%), are good reservoirs for water, hydrocarbons, and CO_2. During last decades, over hundreds of studies about Tahe karst cave reservoir have been reported ranging from structural geology, karstification, reservoir characterization, geomodelling, etc. Xu et al., (2021) present a review of these progresses.

Because of large fluid storage potential of Tahe cave reservoir, abundant geological data and consequent analyses have been obtained, including over 3000 wells, 3D seismic data, outcrop measurements, geomechanical simulation results, fault and fractures interpretation, and karstification history analyses. Although the wealth of data provides a solid foundation for geomodelling of the karst cave reservoir, the sophisticated geological patterns of the cave reservoir and the challenges in expressing complex geological patterns using traditional geostatistics-based geomodelling approaches make it difficult to produce cave reservoir models consistent with expected spatial patterns. For example, Liu et al. (2012) and Lu et al. (2012) utilized variogram-based approaches to simulate cave models, but the simulated caves are distributed in large pieces and cannot show specific shapes. Li et al. (2016a) and Li et al. (2016b) used MPS-based approaches to produce underground river caves of Tahe area; the simulated caves can present a ribbon-like shape to some extent but the continuity and variability still need to be improved. In this paper, we only consider the underground river cave reservoir type (excluding the isolated and fault-controlled cave reservoir types) as an example for geomodelling with the proposed GANSim-3D.

The structure of this paper is organized as follows. Section 2 describes GANSim-3D geomodelling framework and specifies its designs for geomodelling of Tahe cave reservoir. Section 3 constructs conceptual models of Tahe cave reservoirs by integrating field geological patterns. Then in Section 4, based on the conceptual models, a training dataset (training facies models, training well data, and training probability maps) is built. In Section 5, we use the training dataset to train a generator based on the GANSim-3D design and evaluate the generator's ability for geomodelling. Next, in Section 6 the pretrained generator is used for practical uncertainty geomodelling of two field reservoirs with different sizes in the Tahe area. Finally, Section 7 gives conclusions of this study.

2. GANSim-3D and its designs for geomodelling of Tahe cave reservoir

2.1 GANSim-3D

GANSim presented by Song et al. (2021b, 2022) can be used to produce 2D reservoir models of the same size as the training data, in its original form. Supporting Information S2 gives detail about the basic theory of GANSim. Since real reservoirs are 3D and of arbitrary sizes, in this study a 3D framework, GANSim-3D, is proposed to address the concerns of 2D and fixed-size geomdelling based on the previous GANSim.

As illustrated in Figure S2, in the generator of GANSim, the concatenation of a random latent vector and a vector of global features is mapped into a feature vector with a fully connected neural network layer, and the following reshape layer further converts the feature vector into multiple channels of 2D feature maps. However, in GANSim-3D, the input latent vector and global feature vector are transformed into 3D concatenated cubes (i.e., random latent cubes and global feature cubes), and the original fully-connected and reshape layers are replaced by 3D convolutional layers. Now there are only convolutional layers in the generator which enables the geomodelling of flexible sizes, which will be explained in detail in latter paragraphs. In addition, to produce 3D reservoir models and condition to 3D observable data like well data and probability maps resulted from 3D geophysical data, all CNN layers of the generator and the discriminator are set to be 3D, i.e., the kernels of the CNN layers are transformed from 2D into 3D.

Figure 1 shows an example of the architecture design of the generator and discriminator of GANSim-3D, which will be used for field geomodelling of Tahe karst cave reservoirs in following sections. In this example, only well data and probability map are used as conditioning data (i.e., excluding global features). There are two types of pipelines in the generator: main pipeline as the backbone and pipelines for the two types of conditioning data. The main pipeline of the generator is composed of 6 3D 3×3×3 convolutional layers (i.e., the kernel size is 3×3×3) and 4 upsampling layers. The input is 8 channels of 4×4×4-latent cubes each containing 64 latent variables sampled from a standard Gaussian distribution, while the output is a 64×64×64-karst cave facies model. The input conditioning data include 64×64×64-well facies data (a well trajectory indicator and a karst cave facies indicator) and one 64×64×64-probability map of karst cave. They are taken into the main pipeline of the generator through parallel input pipelines of conditioning data that are composed of downsampling layers and 1×1×1 convolutional layers (i.e., the kernel size is 1×1×1). All feature cubes converted from the input conditioning data are set to have 16 channels (e.g., the feature cube with size of 4×4×4×16 or 8×8×8×16). The discriminator is basically symmetrical to the main pipeline of the generator, except that two fully connected layers and one minibatch standard deviation layer are included. All 3×3×3-size convolutional kernels (in the main pipeline of the generator and the discriminator) have a stride size of 1×1×1 and are padded with zeros. The leaky rectified linear unit function (LReLU) with a leaky value of 0.2 is used as the activation function in all layers of the generator and the discriminator except the last layer of the discriminator for which no activation function is used.

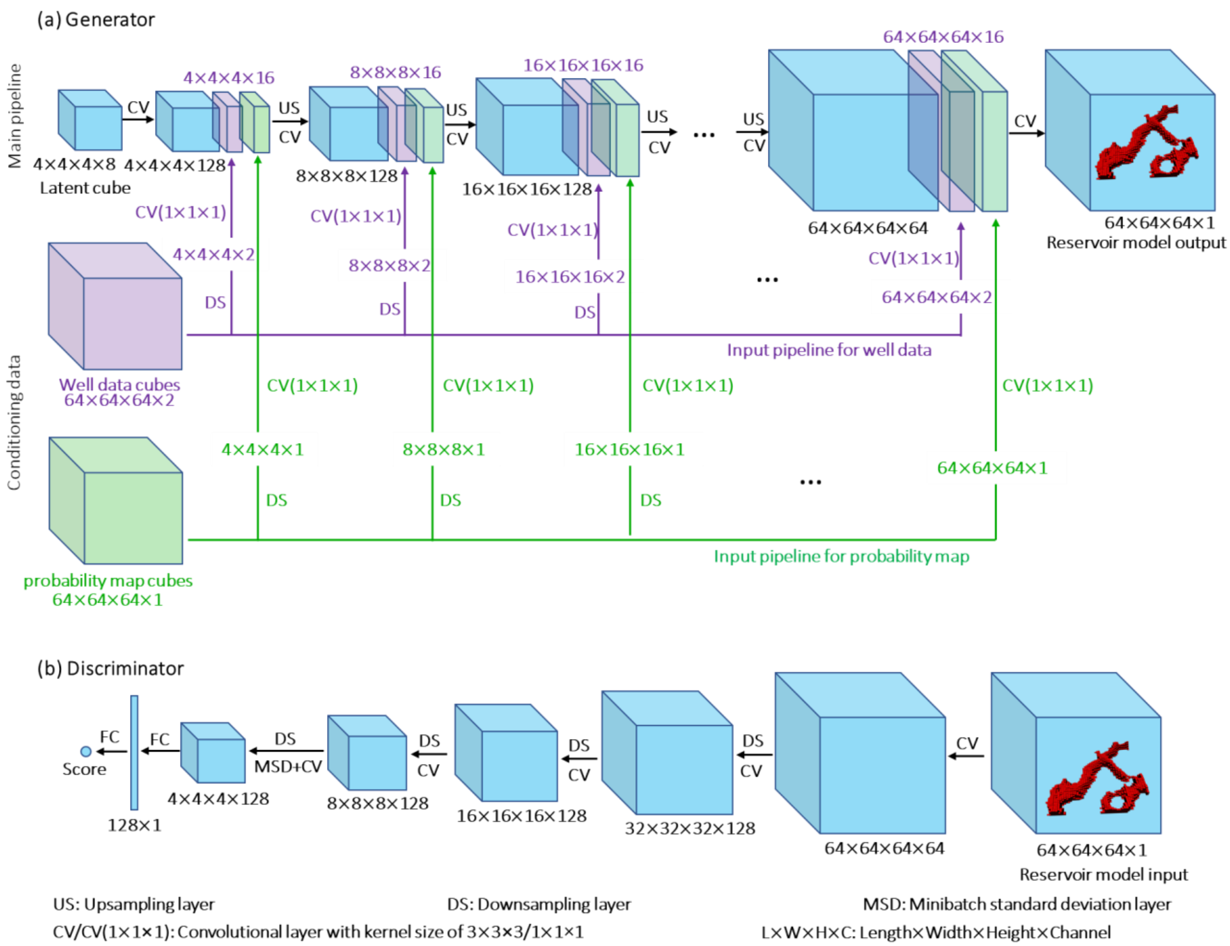

Figure 1 Architectures of the generator and the discriminator used for geomodelling of 3D Tahe cave reservoirs. Only one data cube is shown is this figure; e.g., 4×4×4×8 represents 8 channels of data cube of size 4×4×4, but only one such data cube is drawn. The generator includes one main pipeline and two pipelines of well data and probability map conditioning data. The input of the main pipeline includes 8 channels of 4×4×4-latent cubes, and the output is a 64×64×64-size karst cave facies model. The input well facies conditioning data include one well trajectory indicator and one cave facies indicator both of size 64×64×64. The size of the input cave probability map is also 64×64×64.

With only 3D CNN layers, the generator can be regarded as an amplifier that amplifies small-size input latent cubes and global feature cubes into a large-size facies model by an amplification factor, conditioned to input probability map and well facies data with the same size as the output facies model. Thus, we may first train the generator on a training dataset consisting of small-size data cubes, and then use the trained generator for geomodelling of reservoirs with large arbitrary sizes by expanding the inputs of the generator as long as the quantitative relationship of the inputs sizes remains constant. For example, once trained on 64×64×64-size training data, the generator of Figure 1 can take in 20×15×5-size latent cubes and 320×240×80-size well data and probability maps to produce a 320×240×80-size cave facies model, where the size of the well data, the probability maps, and the output cave facies model is 16 times that of the latent cubes, which is the same amplification factor as the original architecture in Figure 1. This feature is very important in geosciences because, first, it is impossible to train a deep learning model to produce earth models with very large size due to the limitation of training data size and computation resources; second, practical areas of interest can be of many possible sizes. Such technique was initially proposed by Jetchev et al. (2016) and has been used in many geosciences researches (e.g. Laloy et al., 2018; Zheng & Zhang, 2022). We will use this technique for geomodelling of large-size reservoirs in Section 6.2.

The total loss function of GANSim-3D is constructed as the weighted sum of the original adversarial GANs loss, condition-based losses for well data, probability data, and global features:

$$L(G,D)_{total} = \beta_1 L(G,D) + \beta_2 L(G)_w + \beta_3 L(G)_p + \beta_4 L(G)_g, \quad (1)$$

where, $L(G,D)_{total}$, $L(G,D)$, $L(G)_w$, $L(G)_p$, and $L(G)_g$ are the total loss, original GANs loss, and condition-based losses for the input well data, probability maps, and global features, while β_1, β_2, β_3, and β_4 are predefined weights. These two types of losses, GANs loss and condition-based losses, are to enforce the generator to learn the geological pattern knowledge and the correct relationships between various input conditioning data and the output facies model. The Wasserstein loss function with gradient penalty (Gulrajani et al., 2017) is used as the original GANs loss here. For details of these condition-based losses, readers can see Supporting Information S2 or Song et al. (2021b, 2022). To better tune the weights, the four losses at the right-hand side of the equation are normalized into standard Gaussian distributions. During training, the discriminator and the generator are alternatively trained. When training the generator, $L(G,D)_{total}$ is minimized, i.e., the original GANs loss and the other three condition-based losses are all minimized; when training the discriminator, $L(G,D)_{total}$ is maximized, i.e., only the original GANs loss is maximized.

In addition, a progressive training method (Karras et al., 2017) is applied, where the generator and the discriminator are progressively trained from shallow to deep neural network layers and the geological patterns and the relationships are learned from coarse to fine scales by the generator.

After training, when we fix the input conditioning data and randomly change the input latent cubes, the generator can produce multiple 3D facies model realizations that are both realistic and consistent with the input conditioning data. These conditional realistic earth models constitute the uncertainty space of the subsurface reservoir.

2.2 GANSim-3D design for geomodelling of Tahe cave reservoir

The proposed GANSim-3D is specified for uncertainty geomodelling of 3D field cave reservoirs in Tahe area. The architectures of the generator and the discriminator are designed as in Figure 1. Since global features are not used as conditioning data here, their corresponding condition-based loss is not included in the total loss function (Equation (1)). Three types of training data are required: 3D karst cave training facies models of size 64×64×64, 3D training well facies data of size 64×64×64, and 3D training probability map of karst cave of size

64×64×64. The training facies model dataset is the most important because they need to incorporate the field geological patterns of the underground river cave reservoir of Tahe area. In the next two sections, we first construct large conceptual models with size 655×655×64 for the field cave reservoirs by integrating the field geological patterns; then we crop the conceptual models into the required size of 64×64×64 as the training facies models; finally, the training well and probability map data of the same size are obtained from the training facies models.

To speed up the training process, minibatch gradient descent and the Adam optimizer with default parameters (Kingma & Ba, 2014) are used. The generator and discriminator are alternatively trained both with a single minibatch. We use 4 GPUs (NVIDIA Tesla V100-PCIE-32GB), 20 CPUs, and 160G RAM in parallel for training.

The layers of the generator and the discriminator are trained from shallow to deep progressively. Each minibatch is set to include 32 training facies models when training the front 4 convolutional layers; when the last two convolutional layers are activated (i.e. when the 64×64×64-size feature cubes in Figure 1 are produced), each minibatch is set to only include 16 training facies models to save GPU memory. The training schedule includes 5,000 training iterations when only the first convolutional layer is activated, 20,000 training iterations after the second and third convolutional layers are activated, 30,000 iterations when the fourth convolutional layer is activated, and unlimited number of iterations after the following layers are activated. The training stops when the generated cave facies models are realistic (i.e., consistent with expected geological patterns), diverse, and consistent with the input conditioning data.

3. Construction of conceptual models of cave reservoir of Tahe area

To build the training facies model dataset of 64×64×64 cells, large-size conceptual facies models with 655×655×64 cells of the underground river cave of Tahe area are built in this part. First, we propose a process-mimicking simulation approach for underground river caves; second, related parameters of Tahe cave reservoir are prepared; then, these parameters are taken into the process-mimicking approach to simulate a number of conceptual models of Tahe cave reservoir; finally, the geological patterns inside these conceptual models are verified. These large-size conceptual models will then be cropped into training facies models of small size in next section.

3.1 Process-mimicking simulation approach

Conceptual models can be constructed using object-based method (e.g. Mosser et al., 2020; Zhang et al., 2019), process-based method, or process-mimicking method (e.g. Pyrcz & Deutsch, 2014). Process-based methods produce realistic earth models but are too expensive for building a large number of 3D earth models. For example, the process-based model of Li et al. (2020) takes 1-5 days to simulate a single 3D karst model of less than 0.1 million grids using a hydrochemical simulation approach.

Researchers (e.g. Audra et al., 2010; Billi et al., 2007; Boersma et al., 2019; Klimchouk, 2009; Klimchouk et al., 2016) have provided insights about the formation mechanism of underground river karst caves. This involves fluid flow through subsurface fracture systems (occasionally including faults) eroding and scouring the surrounding rocks, often involving chemical dissolution, and finally forming ribbon-like karst caves along the fracture system. Following the formation mechanism, we propose a process-mimicking approach to simulate underground river karst caves (see Figure 2) with the following steps.

(1) Select a cave simulation area. Considering all fracture sets in the area, obtain the fracture density map, the probability density function (pdf) of fracture strike, and the pdf of fracture length for each fracture set. In addition, obtain the vertical profile of the underground river cave to be simulated and the pdfs of cave width and height.

(2) Inside the cave simulation area, randomly select a fracture set and the center of initial fracture according to the fracture density maps.

(3) Based on the pdfs of strike and length of the fracture set, randomly sample the strike and length for the initial fracture. Then construct the initial fracture.

(4) Inside the current simulated fracture, randomly select an intersection point between current and the next fracture to be simulated. From this intersection point construct a new fracture by randomly selecting a fracture set based on the fracture density maps, and again drawing the strike and length randomly from their corresponding pdfs.

(5) Decide if the newly constructed fracture meets the fracture simulation stopping criteria; if yes, stop fracture simulation, otherwise repeat step (4), and (5). The stopping criteria include that, either the newly constructed fracture intersects the boundaries of the simulation area, or the number of simulated fractures reaches a predefined target value.

(6) Considering that underground river cave system may include several branches, for each branch, randomly select one simulated fracture as the initial fracture of this new branch. Then repeat step (4) and (5) to simulate fractures of this new branch.

(7) Randomly trim a fixed proportion (predefined value) of dead ends (the part between fracture end and nearest intersection point) of the simulated fracture system.

(8) According to pdfs of cave width and height, randomly sample width and height values for the cave system. Then based on the cave profile and the sampled cave width and height, expand the fracture system into a 3D cave system.

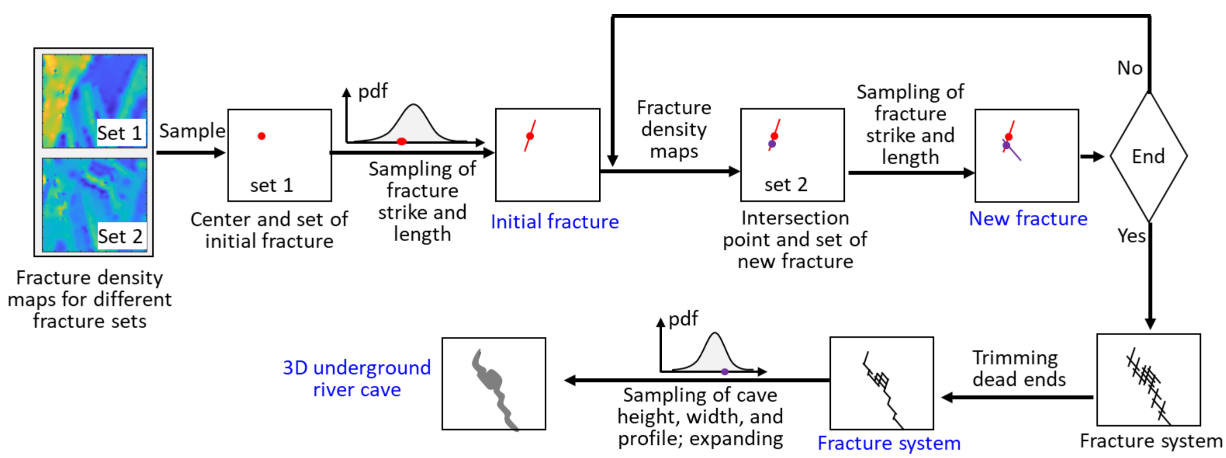

Figure 2 Workflow of proposed process-mimicking approach for underground river cave

3.2 Simulation-related parameters of the Tahe cave reservoir

According to above workflow, we apply this process-mimicking approach to simulate conceptual facies models of underground river cave of Tahe area. There are mainly three sets of fractures with strikes of NNE, NNW, and nearly EW in Tahe cave reservoir. Based on image logs from several wells, the pdfs of fracture strike for the three sets are characterized by von Mises distributions (Berens, 2009; Fisher, 1993) as in Figure 3 (b) with the pdf parameters as given in Table 1. The pdfs of fracture length for the three sets are fit with a power law distribution based on the corrected measurement of outcrop fractures and seismically interpreted fractures presented in Méndez et al. (2020), as shown in Figure 3 (c) and Table 1. We choose a sub-area of 16km×13km inside Tahe area to simulate the underground river cave reservoir. The combined fracture density map of the three fracture sets is calculated from strain energy density distribution (obtained from Geomechanical simulation) and the relationship between the strain energy density and the fracture density estimated from core observation data. This is similar to the approach used in Feng et al. (2018). Here, the three sets of fractures are assumed to occur with the same probability at each point of the simulated fracture density map, so in the next process-mimicking simulation step the center or intersection point of a fracture is first selected according to the combined fracture density map, then one of the three fracture sets is equiprobably decided.

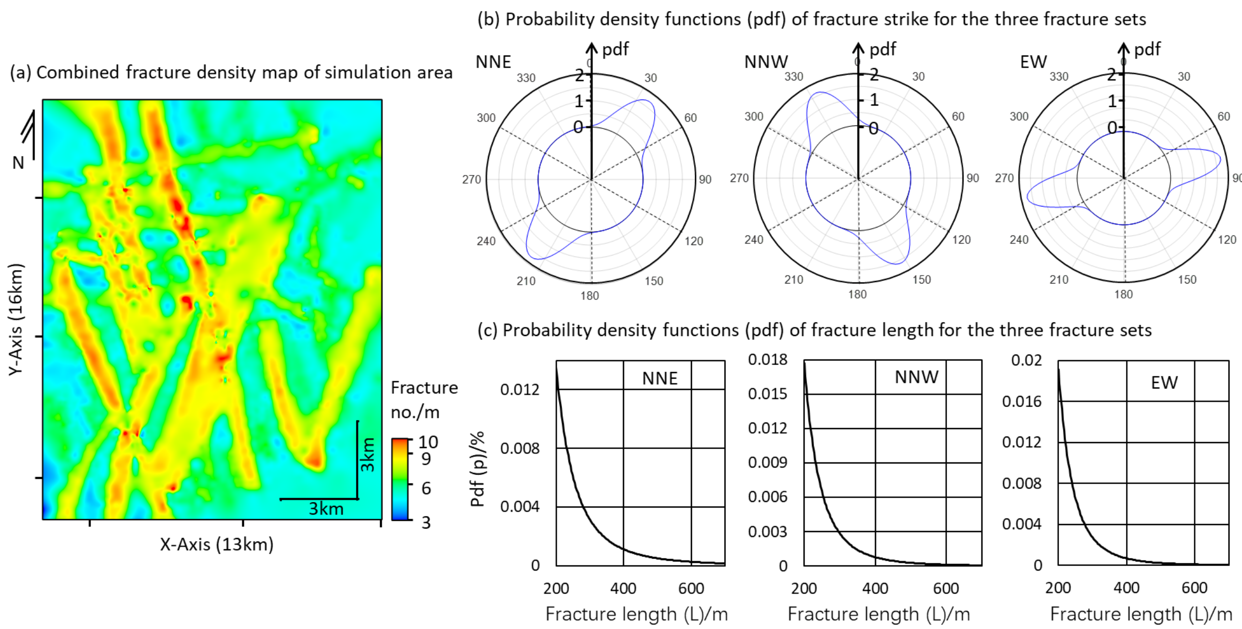

Figure 3 Combined fracture density map, pdfs of fracture strike, and pdfs of fracture length for the three fracture groups of Tahe cave reservoir.

Table 1 Pdfs of fracture strike and length for the three fracture groups of Tahe reservoir.

	Strike (von Mises distribution)		Length (L)		
	Average (μ)/degree	Concentration(κ)	Pdf (p)	Min/m	Max/m

NNE	38（218）	19	$p = 2.6 \times 10^6 \times L^{-3.6}$	200	700
NNW	153（333）	17	$p = 2.6 \times 10^6 \times L^{-4.5}$	200	700
EW	78（258）	31	$p = 2.6 \times 10^6 \times L^{-4.8}$	200	700

Based on outcrop observations of caves in the Tahe area (Figure 4 (a)), we use a half ellipse to approximate the cave profile. The size of outcrop caves (<5m) is usually much smaller than subsurface caves (several to tens meters), because large outcrop caves collapse easily. Thus, it is difficult to obtain the pdf of subsurface cave width from outcrop caves. In our case, we use the pdf of cave height-to-width ratio instead, which is obtained from the measurement of outcrop caves and the vertical sections of seismic attribute data (Figure 4 (b)). The pdf of cave height is fit from the statistics of wells drilled through underground river caves (Figure 4 (c)).

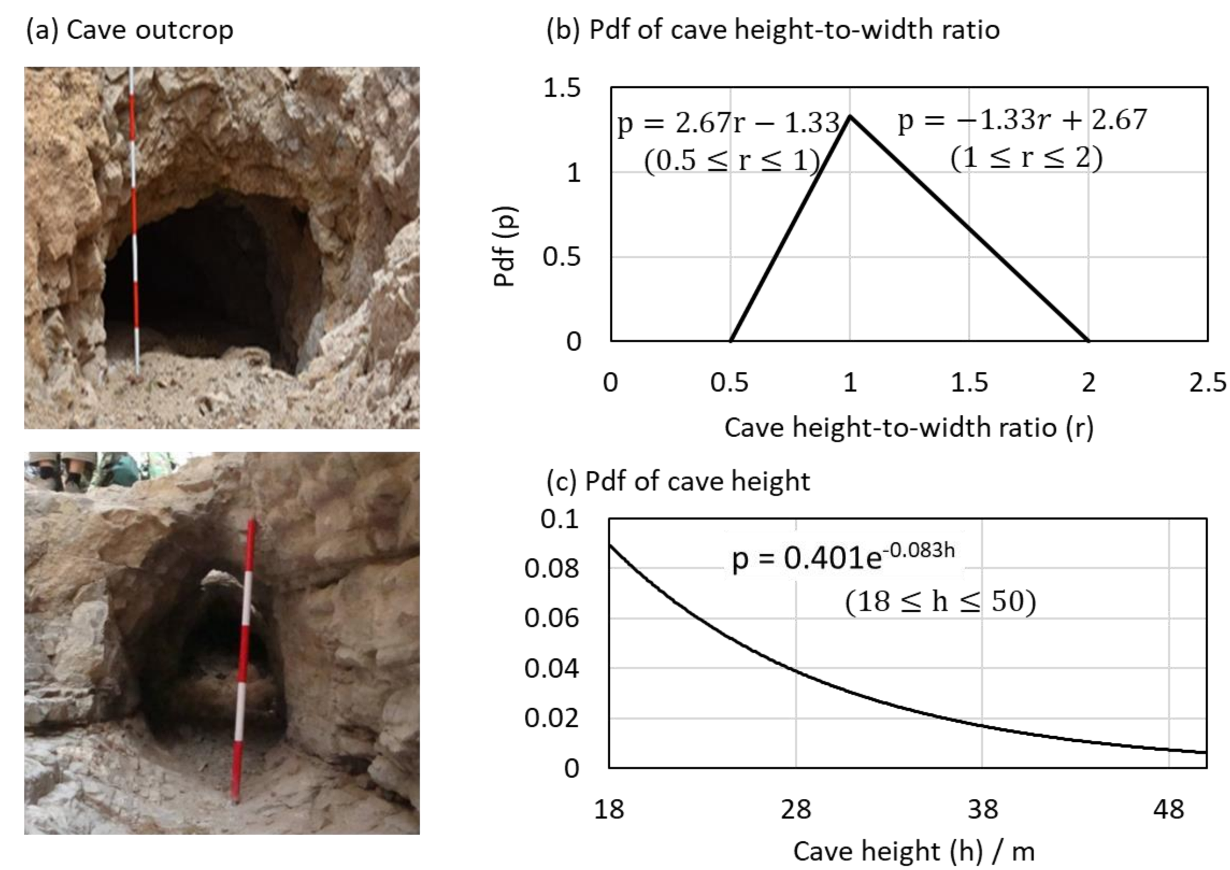

Figure 4 Cave outcrop examples and pdfs of height-to-width ratio and height of underground river cave in Tahe reservoir.

3.3 Simulation of conceptual models of Tahe area

To get different conceptual models of karst cave, in every simulation, we randomly crop a sub-area (8192m×8192m) from the original simulation area (Figure 3 (a); 16km×13km), and use the fracture density map inside the sub-area, pdfs of fracture strike and length, and pdfs of cave height and height-to-width ratio to simulate one conceptual model, based on the proposed process-mimicking workflow. In total, 642 conceptual models of karst caves are simulated; each model includes 655×655×64 cells, and each cell is 12.5m (length) ×12.5m (width) ×1m (height). Figure 5 and Figure 6 show a planer view and vertical sections of one randomly selected simulated model.

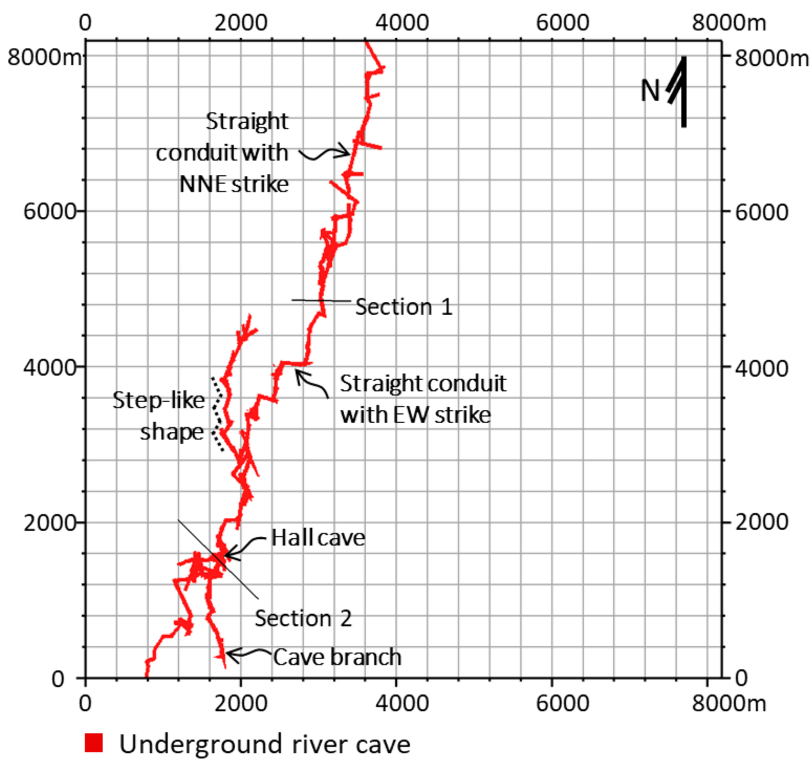

Figure 5 Planer view of one randomly generated conceptual model of underground river cave reservoirs in Tahe area, simulated with the process-mimicking workflow. Only cave facies are shown.

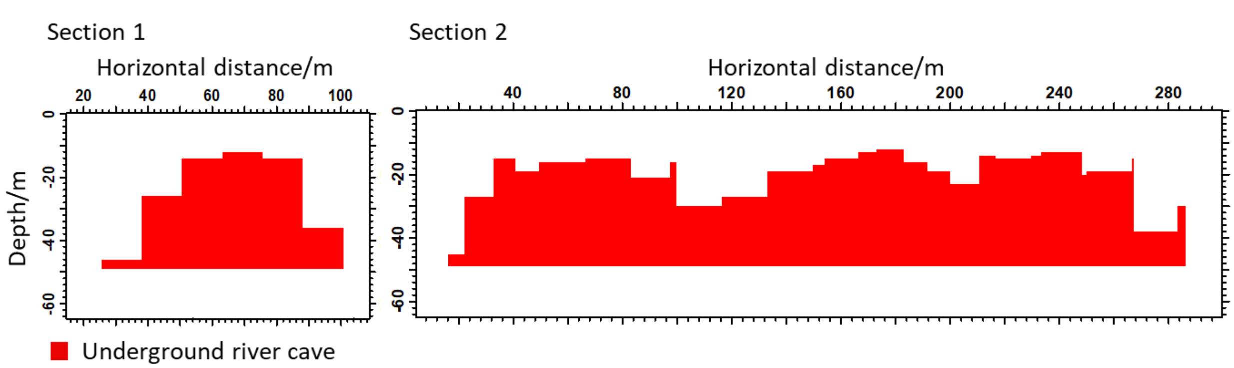

Figure 6 Vertical sections of the randomly generated conceptual model shown in Figure 5. The sections are marked in Figure 5. Only cave facies are shown.

3.4 Verification of geological patterns in simulated conceptual models

As shown in Figures 5 and 6, the simulated caves in these conceptual models are connected, like ribbons. Each cave system is composed of many small straight conduits. Most of these conduits have strikes of NNE, NNW, and nearly EW. A step-like shape can be observed from several connected conduits. Cave branches also develop. Hall caves—cave whose width is several times of normal cave width—are sparsely developed (section 2 of Figure 6). Most caves have a half ellipse profile (section 1 of Figure 6). These are typical features of underground river karst cave of Tahe reservoir. Figure 7 shows a planar section of the seismic frequency energy attribute of a small part of Tahe cave reservoir, where one or two cave systems can be clearly recognized. From the section, we can observe cave conduits with strikes of NNE, NNW, and nearly EW some of which are marked by dashed lines, sparsely distributed hall caves, cave branches, and step-like shape of connected conduits (Figure 7 (b) and (c)), similar to patterns generated. Therefore, we can conclude that the conceptual models simulated by the process-mimicking algorithm integrate the geological patterns of field cave reservoir of Tahe area.

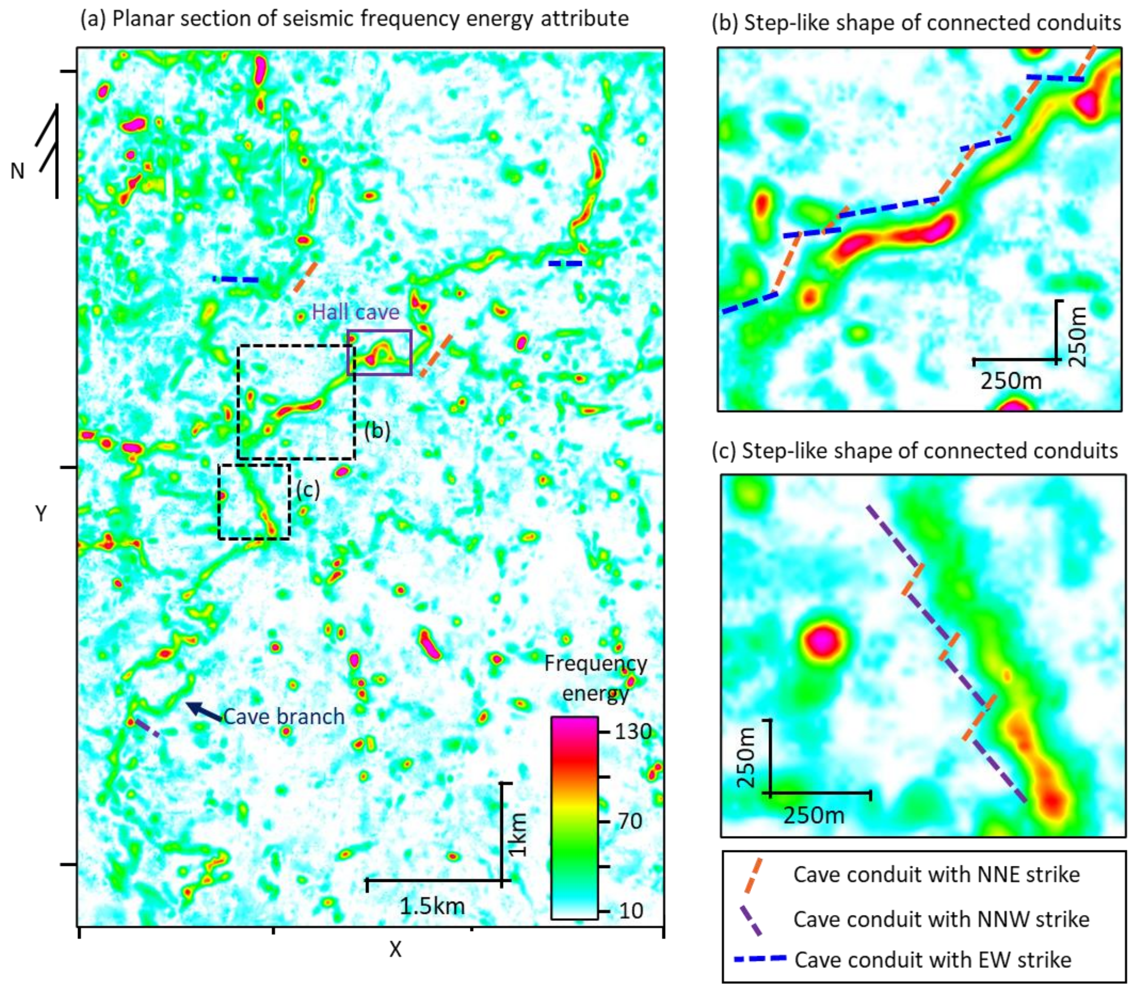

Figure 7 Planar section of seismic frequency energy attribute of a small part of Tahe cave reservoir.

4. Construction of the training dataset

The training dataset includes training facies models (64×64×64), training well facies data (64×64×64), and training probability map of karst cave (64×64×64). We build training facies models from the simulated conceptual models of karst cave reservoir of Tahe area, by randomly cropping the large conceptual models (655×655×64) into blocks of 64×64×64. The training well facies and probability maps data are obtained from these cropped training facies models.

4.1 Training facies models

After randomly cropping the 642 large conceptual models, a total of 22,695 3D training facies models (64×64×64) of underground river karst cave are obtained. Each cell represents 12.5m (length) ×12.5m (width) ×1m (height). Figure 8 shows 9 random training facies models.

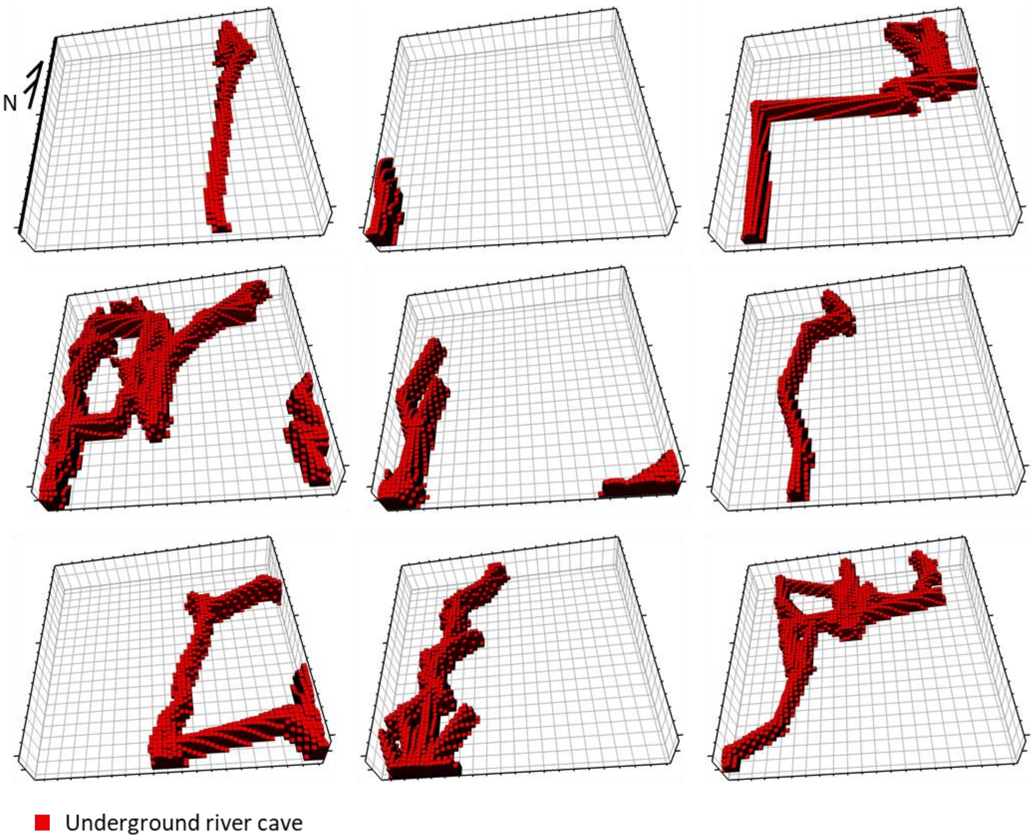

Figure 8 Randomly selected 9 training models of underground river karst cave. Each model has 64×64×64 cells, and each cell represents 12.5m (length) × 12.5m (width) × 1m (height). Only cave facies are shown.

4.2 Training well facies data

Theoretically, when constructing sparse training well data, all types of wells should be considered, including straight wells, inclined wells, horizontal wells, and wells not drilling through a model. In such cases, well data are distributed like strings along well trajectories. To make this process simpler, we ignore the string-like feature of well data and randomly sample sparse cells from the previously constructed training facies models to build training well data. Such non-string-like well data do not exist in practice, but they can help train the generator to condition on normal string-like well data, as is illustrated in the case studies of Section 5 and 6. From each training facies model (with 64×64×64 cells), we sample 1-500 cells to form one set of training well data; the void cells between these sampled cells are set to an easily recognized numeric code for no data, e.g., -99. Finally, 22,695 sets of training well facies data (each with 64×64×64 cells) are built. Figure 9 shows the 9 training well facies data sampled from the facies models in Figure 8.

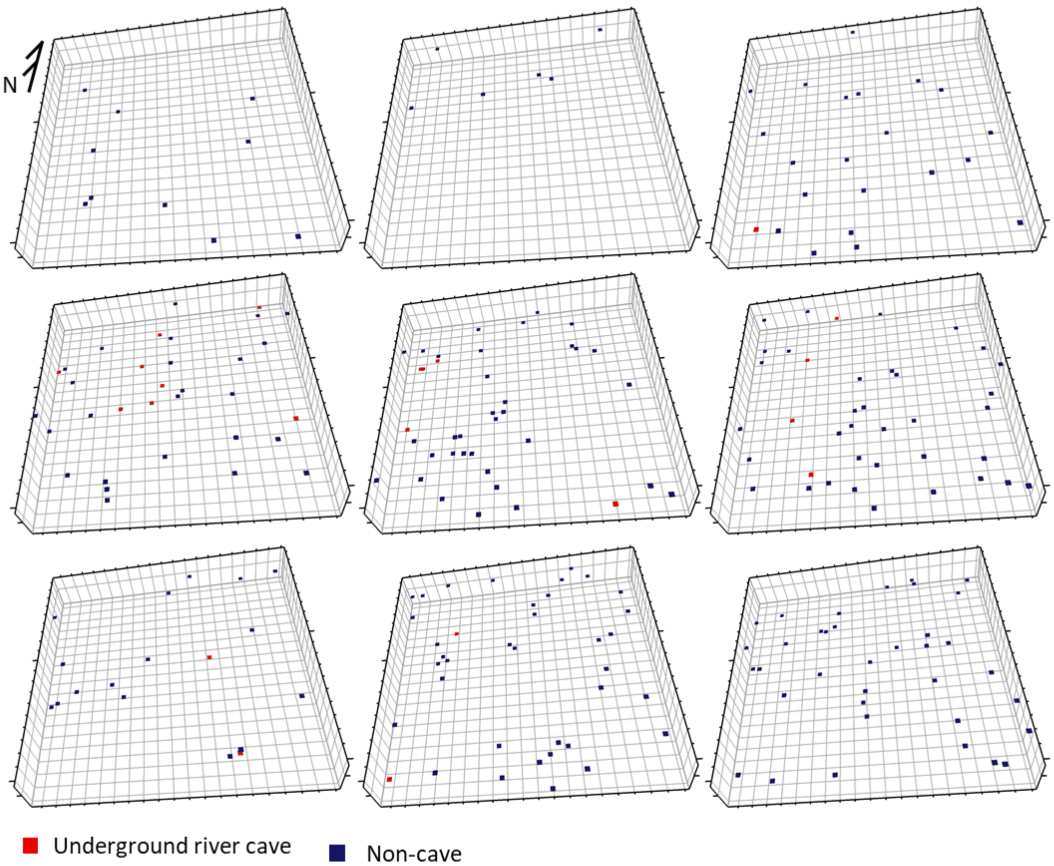

Figure 9 Training well facies data obtained from the 9 facies models in Figure 8. Each set of well data has 64×64×64 cells, and each cell represents 12.5m (length) × 12.5m (width) × 1m (height).

4.3 Training probability map of underground river cave

Training probability map data of underground river cave are also obtained from the 3D training facies models using a Gaussian smoothing approach, to mimic real geophysically interpreted probability maps. First, the facies models are preprocessed into indicator models of karst cave: the karst cave cells are set to be 1 while other cells are set to be 0. Second, these indicator models are smoothed using 3D Gaussian kernels with sizes of 4×4×50, 6×6×75, 8×8×100, or 10×10×125 to form 3D probability map of underground river caves with dimensions of 64×64×64. Here, different kernel sizes are used in order to make the training probability maps similar to the practical ones (obtained from geophysical data) which may have diverse resolutions (blurriness). The vertical size of these kernels is 12.5 times of horizontal size, because the horizontal size (12.5m) of each cell is 12.5 times of the vertical size (1m). Third, 5% - 30% of Gaussian noise are randomly added into each probability map to mimic practical probability map data in which noises are inevitably introduced. Due to the added noise, the constructed training probability map data may not be strictly consistent with the training well facies data, e.g., karst cave cells in well data may correspond to low probability value in probability map data and vice versa. Such phenomena are common in practice. Finally, 22,695

3D probability map data are constructed. Figure 10 shows the 9 training probability maps calculated from the 9 facies models of Figure 8 with different Gaussian kernels.

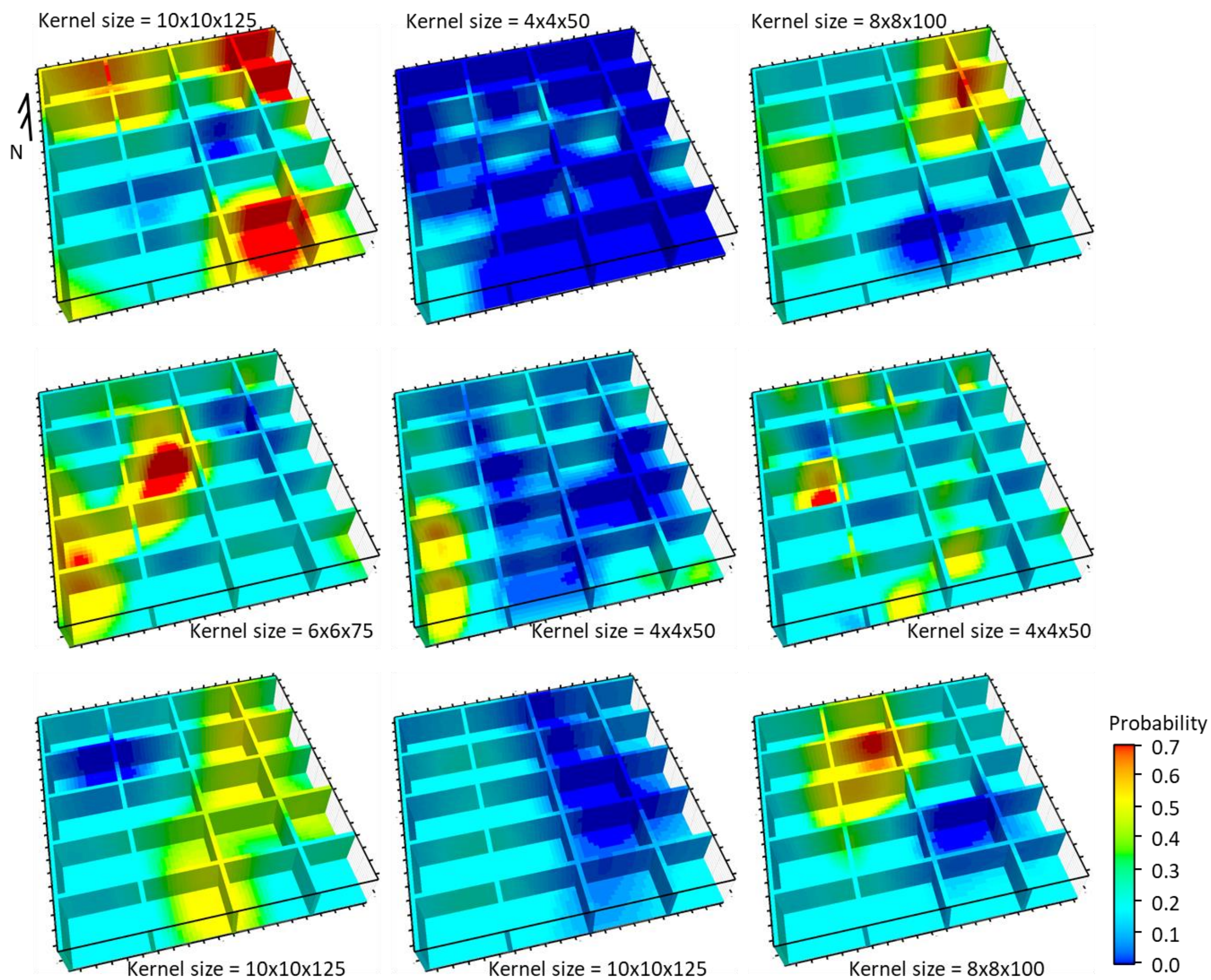

Figure 10 Training probability maps obtained from the 9 facies models in Figure 8 using Gaussian kernels of different sizes. Each probability map has 64×64×64 cells, and each cell represents 12.5m (length) × 12.5m (width) × 1m (height).

Among the 22,695 training facies models, well data, and probability maps, 20,000 are used for training GANs, while the remaining 2,695 are used as test dataset to evaluate the trained generator.

5. Training and evaluation of the generator

5.1 Training of generator

The weights for the three of losses (i.e., β_1 for GANs loss, β_2 for well condition-based loss, and β_3 for probability map condition-based loss in Equation (1)) are investigated through trial-and-error experiments as in Song et al. (2021b). Supporting Information S4 shows the produced results of trained generators for various combinations of the weights. We suggest setting weight β_2 and weight β_3 between 0.07 to 0.35 and 0.5 to 2.5, while setting weight β_1 as 1. The weight β_2 represents a tradeoff between the conditioning of well data and the realism of the earth models produced by the trained generator, while β_3 represents a tradeoff between the diversity and the realism of the produced earth models. In this paper, we set β_1, β_2, and β_3 as 1, 0.35, and 0.5, respectively. With other settings as in Section 2.2, the generator was trained for 40 hours until the generated facies models were visually realistic, diverse, and conditioned to input well and probability map data. The trained generator takes random latent cubes, 3D well facies data, and 3D probability map as inputs and produces multiple 3D facies models of underground river karst cave systems.

In Section 5.2, we first evaluate the trained generator in two synthetic cases in terms of the realism, diversity, conditioning to input well facies and probability map, and prediction accuracy of the simulated realizations. Then in Section 6, we use the trained generator for uncertainty geomodelling of field karst cave reservoirs of Tahe area.

5.2 Evaluation of the pretrained generator based on synthetic cases

We chose two random facies models from the test dataset (not used for training) as the ground truth and obtained two groups of corresponding 3D probability maps of karst cave and well facies data via Gaussian smoothing (as described in Section 4.3) and random sampling. The pretrained generator takes in 400 groups of random latent cubes (each group has 8 channels of $4\times4\times4$-latent cubes), the probability map, and the well data to produce 400 facies model realizations for each synthetic case. Each realization has $64\times64\times64$ cells, and each cell represents 12.5m (length) $\times$ 12.5m (width) $\times$ 1m (height). Figure 11 and Figure 12 show the ground truth facies model, input 3D probability map, input well data, and 5 realizations for each synthetic case. It takes 0.02 seconds to produce one realization on 1 GPU (V100).

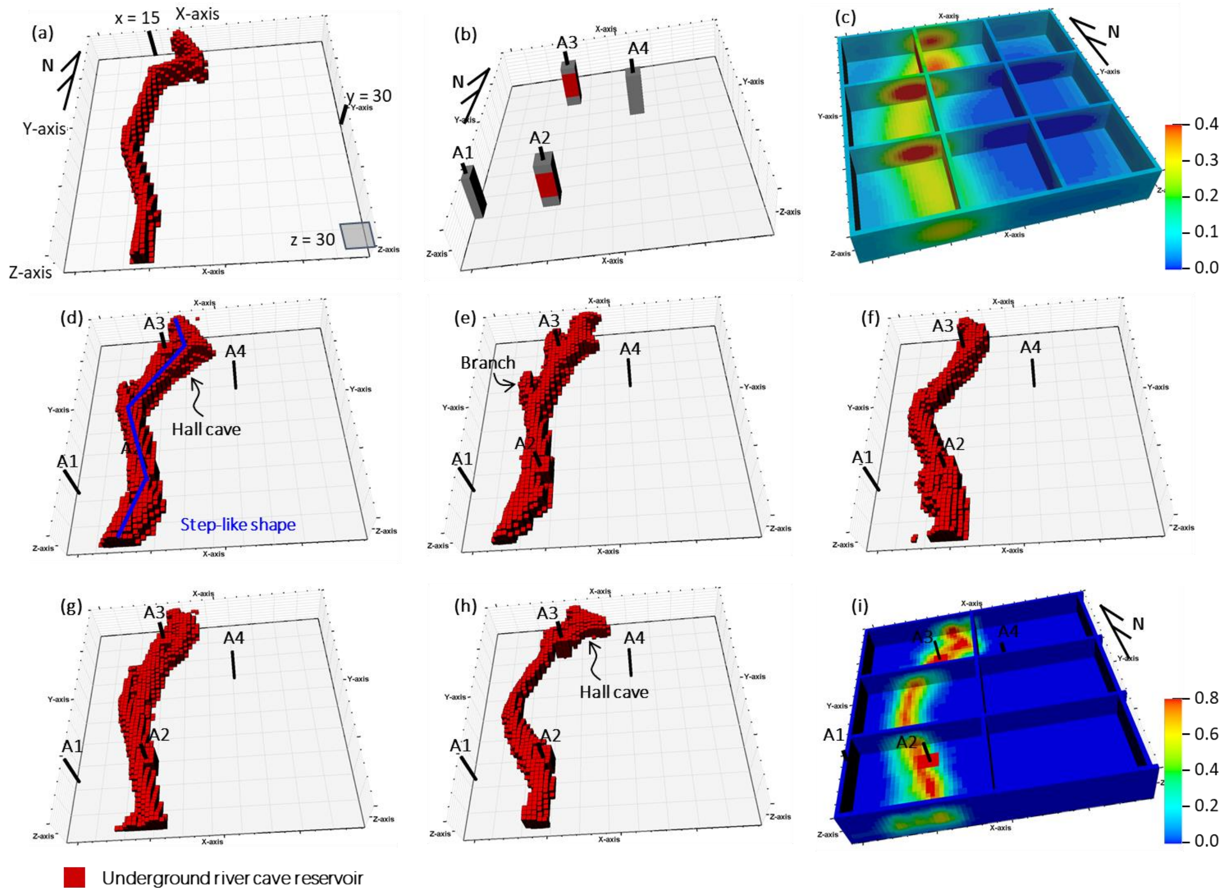

Figure 11 Geomodelling results for synthetic case 1. (a) Ground truth karst cave facies model; (b) Sparse well facies data sampled from the ground truth facies model (the gray cells represent non-cave facies type); (c) Probability map of karst cave obtained from the ground truth via smoothing; (d) – (h) Random facies model realizations directly produced from the pretrained generator by taking the well data and probability map as conditioning inputs; (i) Frequency map calculated from 400 generated realizations. All subfigures include 64×64×64 cells, and each cell represents 12.5m (length) × 12.5m (width) × 1m (height). Only karst cave cells are shown.

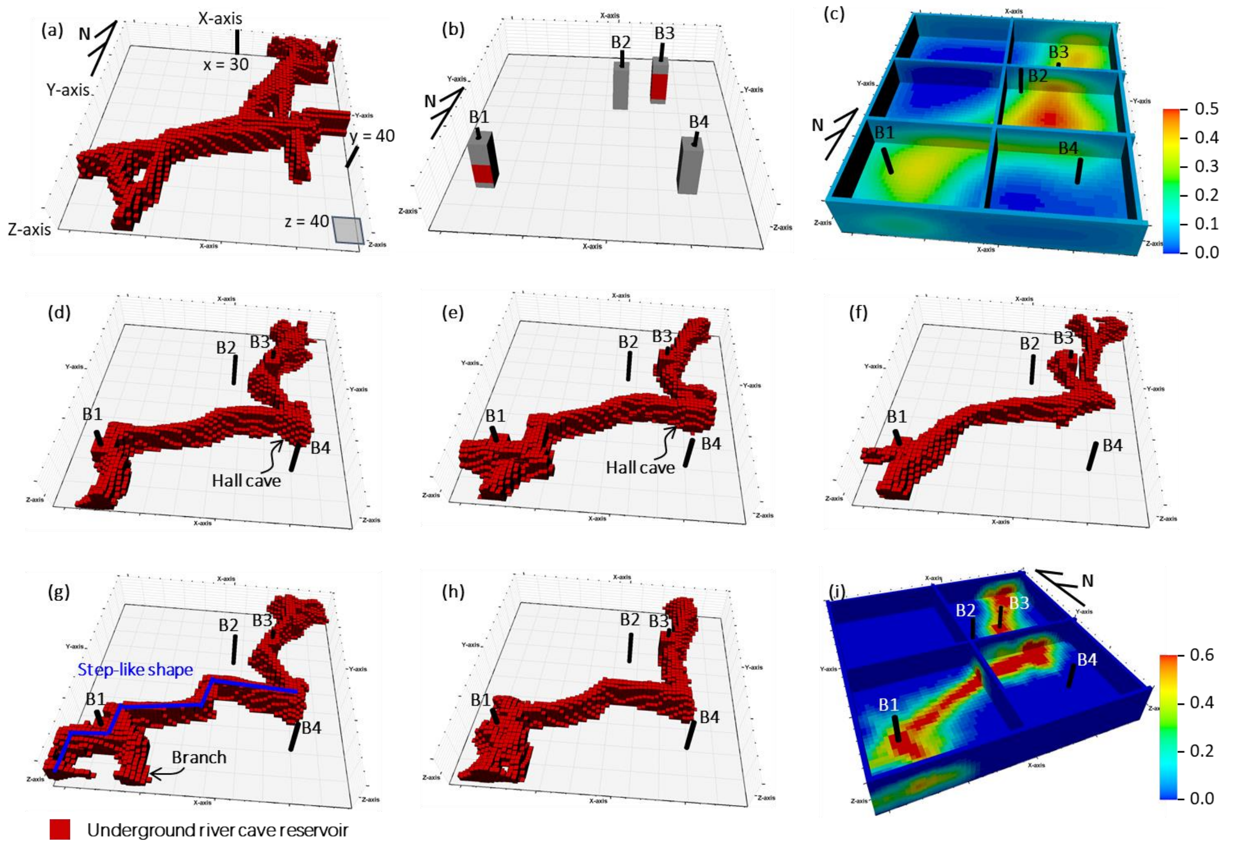

Figure 12 Geomodelling results for synthetic case 2. (a) Ground truth karst cave facies model; (b) Sparse well facies data sampled from the ground truth facies model (the gray cells represent non-cave facies type); (c) Probability map of karst cave obtained from the ground truth via smoothing; (d) – (h) Random facies model realizations directly produced from the pretrained generator by taking the well data and probability map as conditioning inputs; (i) Frequency map calculated from 400 generated realizations. All subfigures include 64×64×64 cells, and each cell represents 12.5m (length) × 12.5m (width) × 1m (height). Only karst cave cells are shown.

From Figure 11 and Figure 12, we can see that these generated karst cave facies model realizations are very realistic, i.e., having very similar geological patterns to the practical karst caves of Tahe area or the training/testing facies models. For example, these simulated underground river caves have a connected ribbon-like shape in planar view and a half-elliptical shape in vertical section, some cave branches develop ((d) and (e) of Figure 11, (e), (f), and (g) of Figure 12), wide hall caves are sparsely distributed ((d) and (h) of Figure 11, (d), (e), and (h) of Figure 12), most straight conduits have strikes of NNE, NNW, and nearly EW, and the step-like shape can be observed from some connected cave conduits (blue lines in (d) of Figure 11 and (g) of Figure 12). These features are very typical in the actual karst caves (Figure 7 and Figure 4) and training/test facies models (Figure 8) of Tahe area.

To quantitatively assess the relationship of internal geological patterns between the generated realizations and the training/test facies models (representing actual karst cave geological patterns), we used Multi-Scale Sliced Wasserstein Distance combined with Multi-

Dimensional Scaling (MS-SWD-MDS) approach to map every facies model into a point in a reduced-dimension 2D space representing its geological pattern. Song et al. (2021a) describe this approach in detail. Supporting Information S3 also explains this approach. Figure 13 (a) and (c) show such point distributions of 100 test facies models, 40 generated realizations, and the ground truth facies model for the two synthetic cases; Figure 13 (b) and (d) show the density contours of these points, which approximate the distributions of underlying geological patterns in a 2D space. From Figure 13, we can clearly see that, first, the geological pattern distribution of the generated realizations is located inside that of the test facies models; second, the former one shrinks to cluster closely around the ground truth facies model. This proves that the generated realizations can reproduce geological patterns of practical karst caves (represented by test dataset) but is constrained due to the conditioning effect of the input probability map and well data. In addition, these realizations are very diverse, which can be seen from Figure 11, Figure 12, and Figure 13.

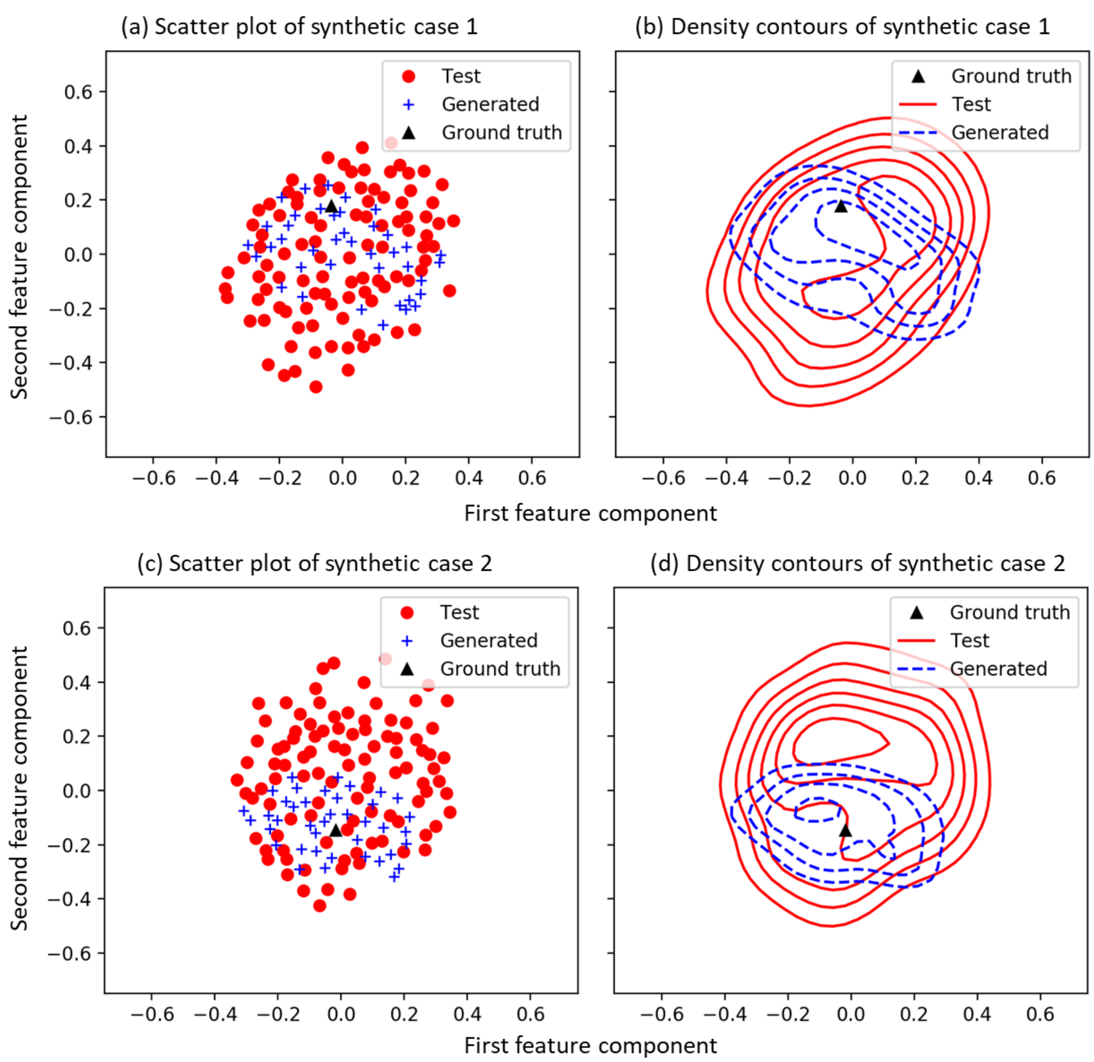

Figure 13 Projection of test facies models, generated conditional facies model realizations, and the ground truth facies models in a 2D space, based on MS-SWD–MDS approach; each point

represents geological patterns of one facies model. (a) and (c) are the point scatter plots of the two synthetic cases; (b) and (d) are the density contour maps obtained from the point scatter plots of the two cases.

Based on the generated realizations, the reproduction accuracy of the input well facies data was 100% for both cases. From careful visual inspection, we can see the locations and shapes of the generated realizations are consistent with the input probability map very well. In Figure 11 and Figure 12, we obtain frequency maps of karst cave from the 400 generated realizations by calculating the proportion of simulated cave among all realizations at each cell (see Equation (S2-5)). The frequency maps are quite similar with the input probability maps. Figure 14 and Figure 15 compare the distributions of input probability map, frequency map, and the ground truth facies models at different sections of the two synthetic cases. Apparently, the generated frequency maps are more concentrated inside the input probability maps towards the ground truth facies models. Especially, some features about the ground truth facies models are lost in the input probability maps but are recaptured in the calculated frequency maps; for example, in Figure 14 (b) and Figure 15 (a), high values of the frequency maps are concentrated around the two ground truth karst caves, although the probability maps give no hint about the number of the ground truth caves; in planar sections of Figure 14 (c) and Figure 15 (c), large parts of the ground truth caves are outlined by the frequency maps. These discussions prove that, (1) the generated realizations are consistent with the input probability maps, and (2) compared to the case of geomodelling only using probability map (where the frequency map completely overlaps with the probability map), the generator's prediction accuracy of caves are largely increased and the uncertainty is decreased. The increased accuracy or decreased uncertainty results from the integration of well data and geological patterns; the difference between the input probability map and the frequency map points to the value of input well data and geological patterns.

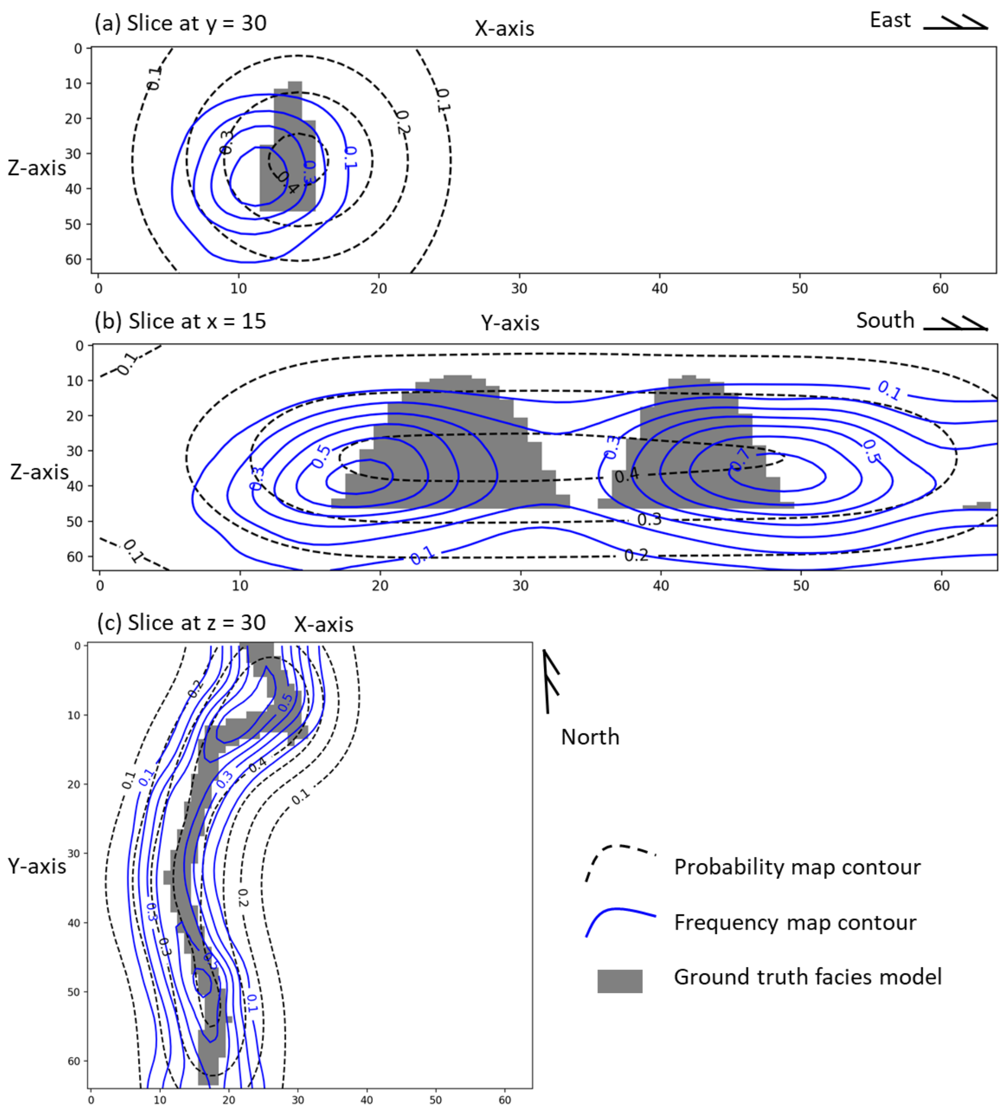

Figure 14 Comparison of input probability map contour, frequency map contour, and the ground truth facies model for synthetic case 1 at three different sections (i.e., y = 30, x = 15, and z = 30). These sections are marked in Figure 11.

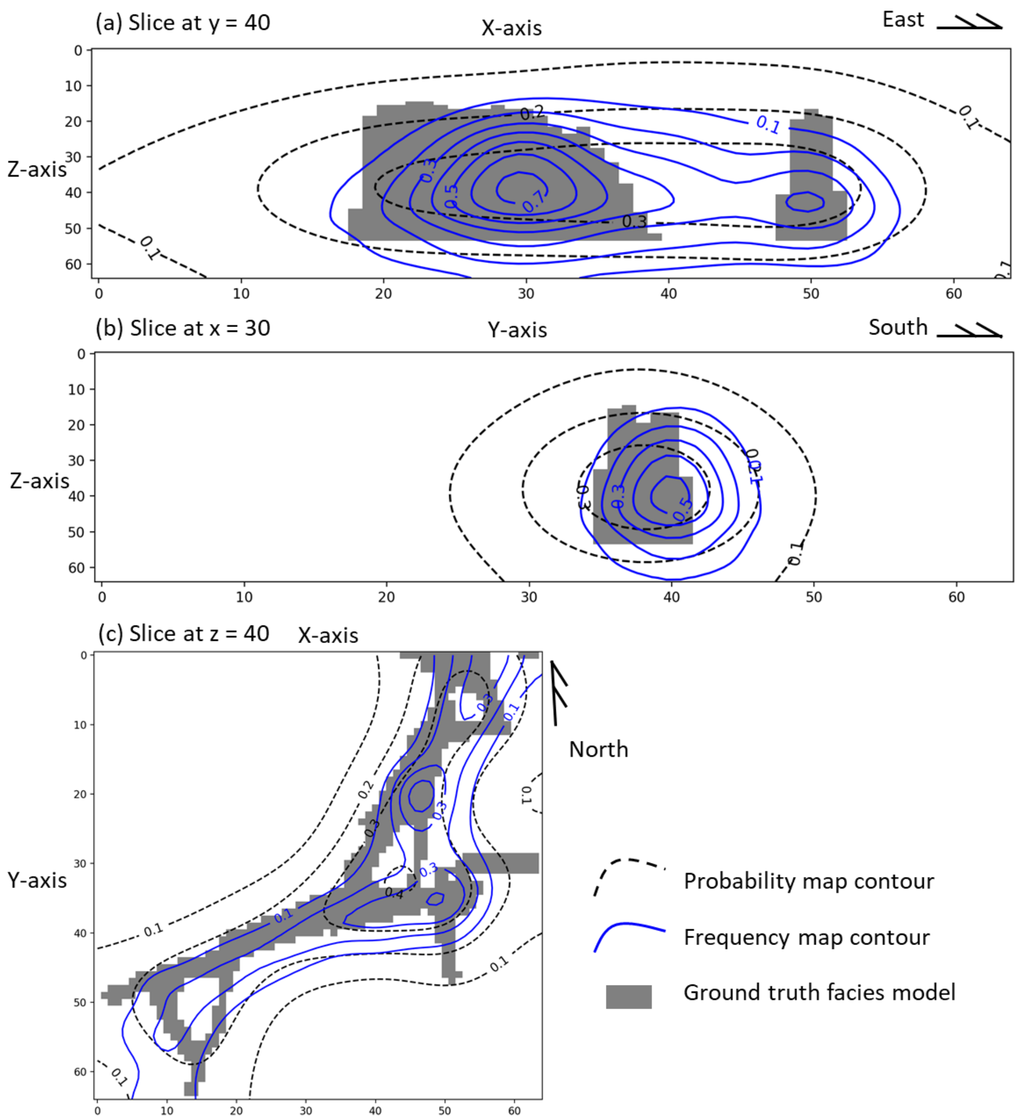

Figure 15 Comparison of input probability map contour, frequency map contour, and the ground truth facies model for synthetic case 2 at three different sections (i.e., y = 40, x = 30, and z = 40). These sections are marked in Figure 12.

Figures 11, Figure 12, and Figure 13 show that the simulated facies model realizations are very close to the ground truth with respect to geological patterns and locations. To quantitatively assess the cave prediction accuracy of these generated realizations, we define intersection-over-union (IOU) metric as cave intersection divided by cave union between one generated (or test) facies model and the ground truth one. IOU varies from 0 to 1; the larger the IOU value is, the more accurate the generated (or test) facies model is. We calculate IOU for the 400 generated realizations (IOU_g) and IOU of 400 random test facies models (IOU_t) as a comparison in both synthetic cases. Figure 16 shows the histograms of IOU_g and IOU_t for the two cases. Most IOU_g values are much larger than most IOU_t values; the maximum IOU_g values are 0.48 and 0.43 in case 1 and case 2. This means that the generated conditional facies models are much more accurate than random unconditional facies models. Figure 17 compares the generated realizations with IOU = 0.2, 0.3, and 0.4 and the ground truth ones for both cases. In addition, the conditioning approach for global features (Song et al., 2021b) could be used to condition the width and proportion of caves, thus further improving the accuracy of simulated realizations.

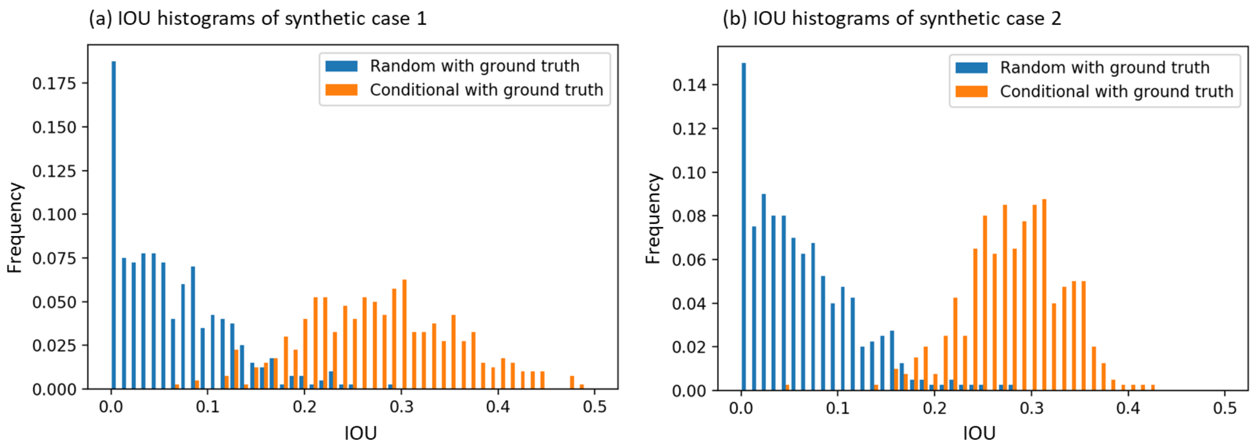

Figure 16 Comparison of IOU histograms between random test facies models and produced conditional realizations for both synthetic cases.

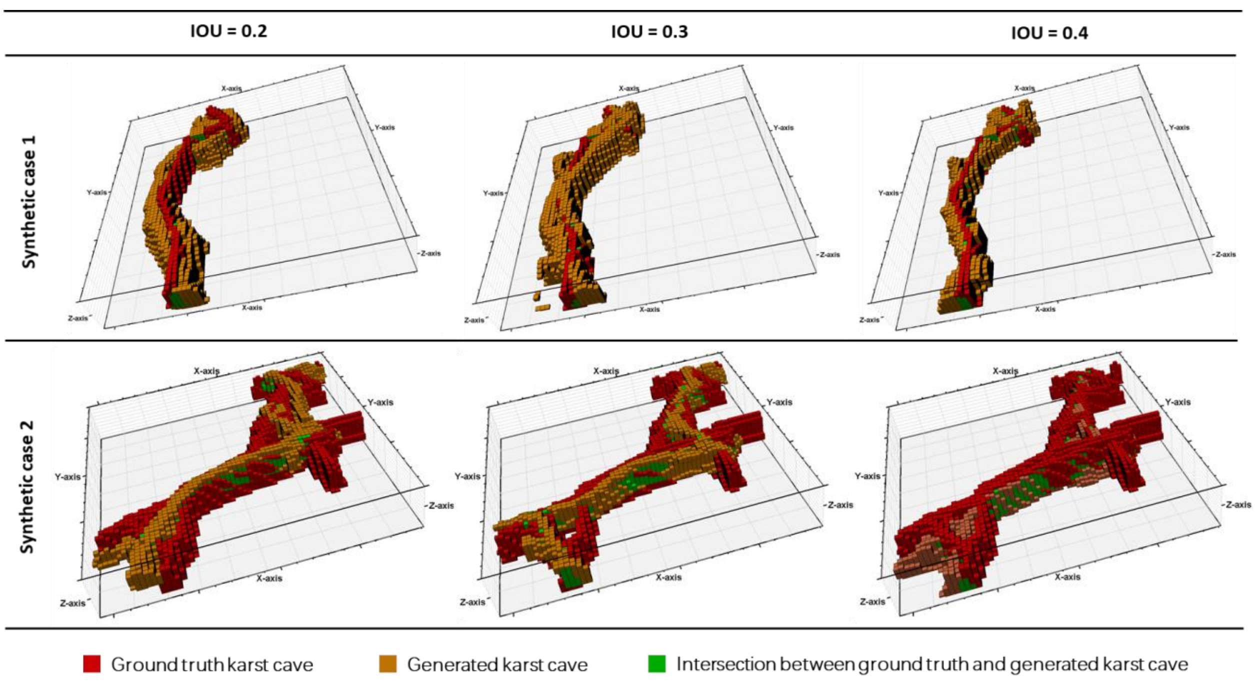

Figure 17 Comparison between the generated karst cave facies models with IOU = 0.2, 0.3, and 0.4 and the ground truth ones for the two synthetic cases. Only karst cave cells are shown.

The above analyses of synthetic cases show that given observed well data and probability maps (calculated from geophysical data), the pretrained generator can quickly produce diverse realizations that are consistent with both the expected geological patterns and the input conditioning data, with acceptable accuracy. Thus, we can rely on the pretrained generator for real field case uncertainty geomodelling, i.e., to produce multiple facies model realizations to represent the uncertainty of real reservoirs. However, how many realizations should be produced? This question is addressed by examining the change in the frequency map with increasing number of realizations. The frequency map changes with increasing number of realizations generated, until for a large enough set of realizations the frequency map converges and does not change anymore. When the frequency map stabilizes, the number of realizations are taken to be enough to represent the uncertainty of the reservoir model. We define a frequency map difference (FMD) as

$$FMD = \sum_{all\ cells}(FM_{x+10} - FM_x)^2, \tag{2}$$

where x is the realization number, FM_{x+10} and FM_x are the frequency map for $x + 10$ and x realizations, respectively. Thus, FMD represents the frequency map change with every 10 new additional realizations produced. Figure 18 shows the FMD change with the number of realizations for the two synthetic cases. The FMD converges to 0 when 200 realizations are produced in both cases, indicating a stable frequency map after that. Thus, we suggest producing 200 facies model realizations when using the pretrained generator for practical uncertainty geomodelling.

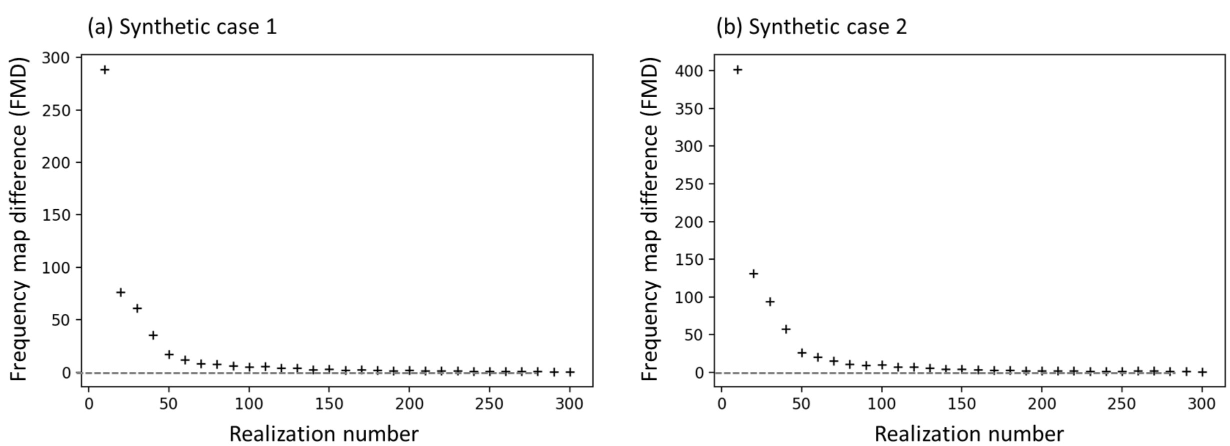

Figure 18 Change of frequency map difference (FMD) for every ten new realizations.

6. Uncertainty geomodelling of field reservoirs with the pretrained generator

We show two field reservoir cases from Tahe area: the first reservoir case is based on 64×64×64 cells (i.e., 800m×800m×64m) – the size at which the generator is trained, while in the second case, we apply the pretrained generator to simulate geological models of 336×256×96 cells (i.e., 4200m×3200m×96m).

6.1 Field case 1 based on 64×64×64 cells

We choose a study area of 800m×800m, with three wells, from Tahe area. The well logs are shown in Figure 19 (a), from which we can recognize a 21m-thick underground river cave interval in well T1 (i.e., 84m to 105m beneath the paleo-geographic surface below which the caves were formed) and no caves in the other two wells. The geo-space of this area between 67m to 131m beneath the paleo-geographic surface is divided into 64×64×64 cells, with each cell representing 12.5m (length) × 12.5m (width) × 1m (height) which is the same as the training/test dataset. Figure 19 (b) shows the distribution of well data in this geo-space. The 3D probability map of underground river cave is calculated from a 3D seismic attribute (frequency energy) and the relationship between that attribute and cave occurrence probability obtained from the statistics of the 3000 wells in Tahe area. Figure 20 shows the probability map of this study area.

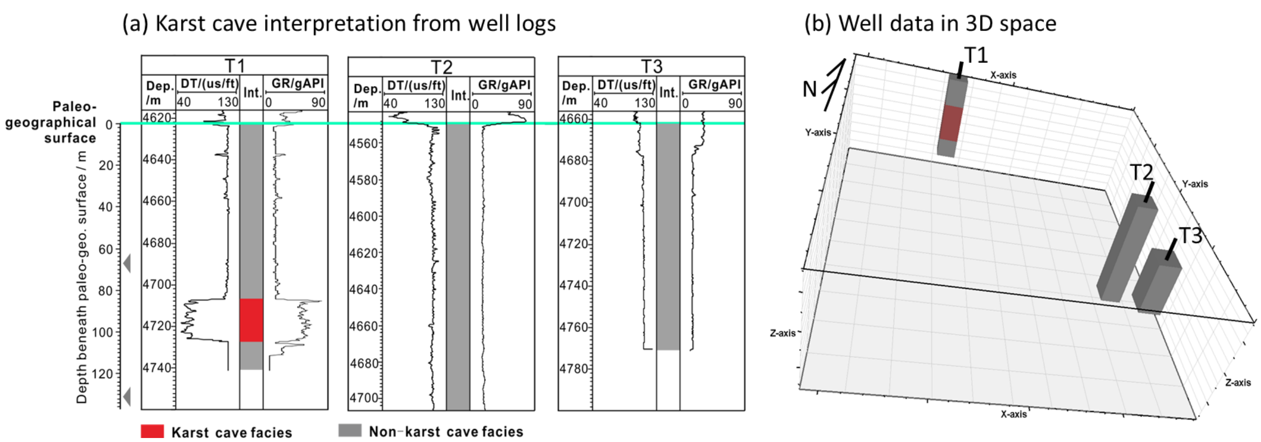

Figure 19 (a) Karst cave interpretation from well logs for the three wells of the study area. (b) Distribution of well facies data in the 3D 64×64×64-cell geo-space (800m×800m×64m) of the study area.

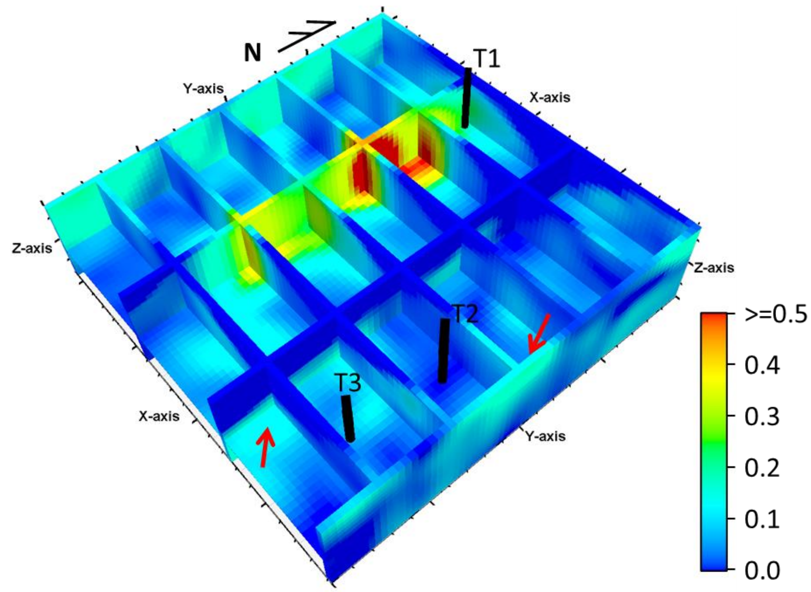

Figure 20 3D probability map of underground river cave for the study area. The map is calculated from the seismic frequency energy attribute and the relationship between that attribute and cave occurrence probability. Red arrows show local high probability areas away from the main trend.

We take the interpreted 3D well facies data, 3D probability map data, and 200 groups of random latent cubes (each group has 8 channels of latent cubes with size of 4×4×4) into the pretrained generator to produce corresponding 200 karst cave realizations. Figure 21 shows 9 of them. Like the previous synthetic cases, the cave systems of these realizations are consistent with expected geological patterns, such as step-like shape (Figure 21 (a)), NNE, NNW, and nearly EW strikes of single conduit, sparse hall caves (Figure 21 (d)).

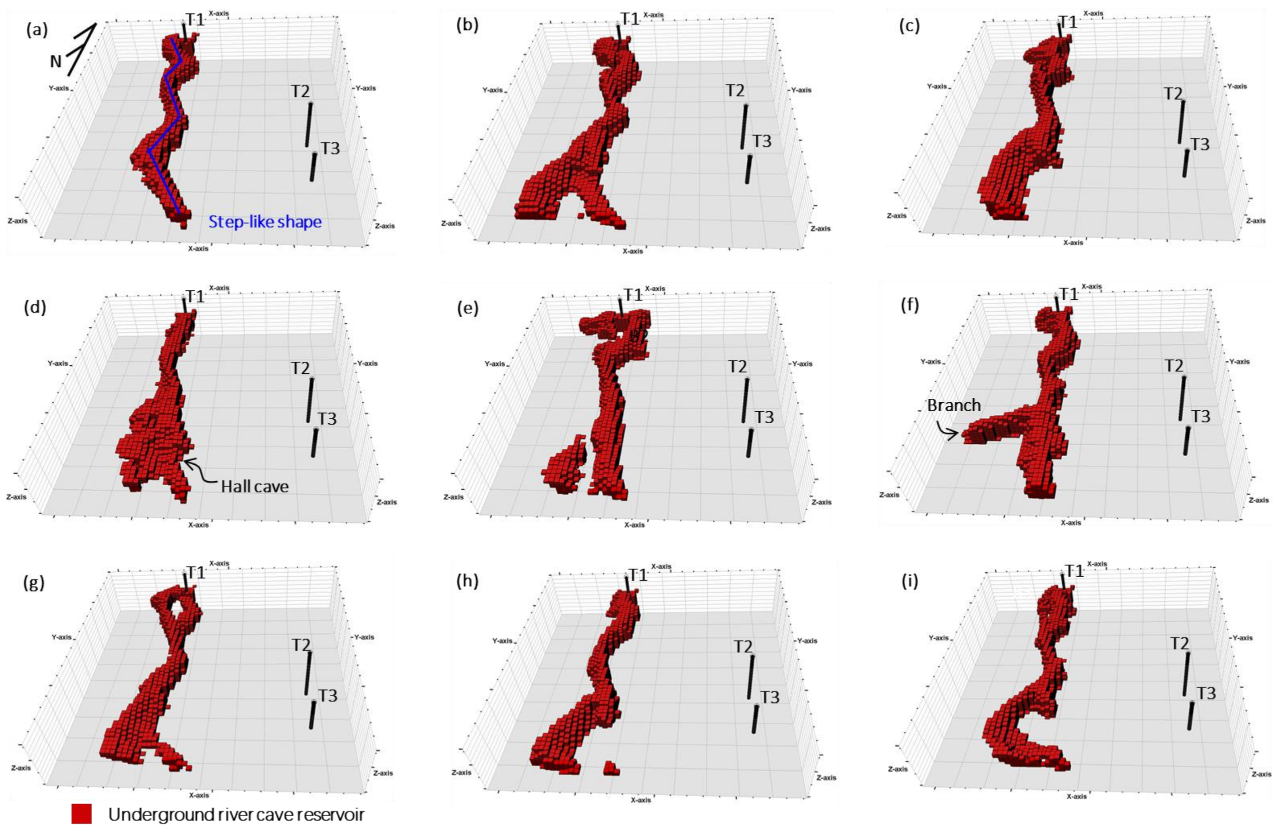

Figure 21 Nine facies model realizations (out of 200) of underground river karst cave for the study area. Each realization has 64×64×64 cells. Only underground river cells are show.

We calculate the frequency map of karst cave from the 200 simulated realizations (Figure 22). By comparing Figure 21 and Figure 22 to Figure 20, we can clearly find that, first, the high value of the probability map is mainly distributed in the slightly west area with a north–south trend, and most simulated caves are also distributed in the same high-probability area and with a north–south trend; second, the high values of the frequency map are concentrated inside the high value area of the input probability map. Therefore, we can conclude that the simulated caves are consistent with the input probability map. By calculation from the 200 realizations, the reproduction accuracy of the input well data is 100%.

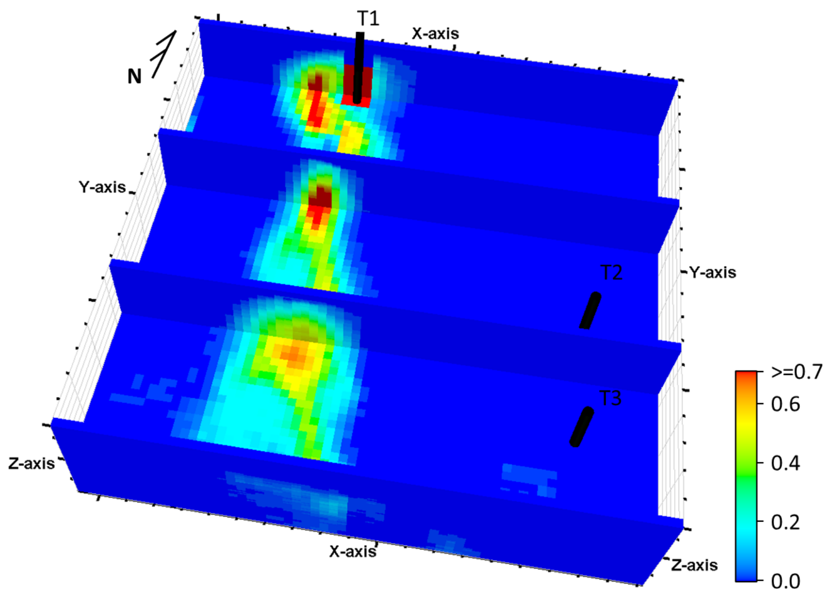

Figure 22 Frequency map of karst cave for the study area calculated from 200 facies models realizations.

In the input probability map, except the major high-value area (slightly west; with value larger than 0.2), there are still other local high-value areas (red arrows in Figure 20). These local areas may result from the noise of seismic data collection, processing artifacts, interpretation uncertainties, or the isolated karst cave type that is not considered in this study. Regardless of causes, these local highs can all be regarded as noises in the background of simulating underground river caves. However, when comparing Figure 20, Figure 21, and Figure 22, we can find that these local noises have completely no effect on the distribution of simulated caves. The reason might be that the spatial shape of these local highs is inconsistent with the ribbon-like geological patterns of underground river caves learned by the generator. Thus, these local non-ribbon-like features of the input probability map are suppressed by the pretrained generator.

The calculated frequency map reveals the "sweet spots" of this area. Figure 23 filters the frequency map based on various thresholds. These filtered frequency maps can be used as inputs for designing well trajectories, calculating reserves of fluids in the cave reservoir, and evaluating the uncertainty of investment and revenue in a more systematic manner.

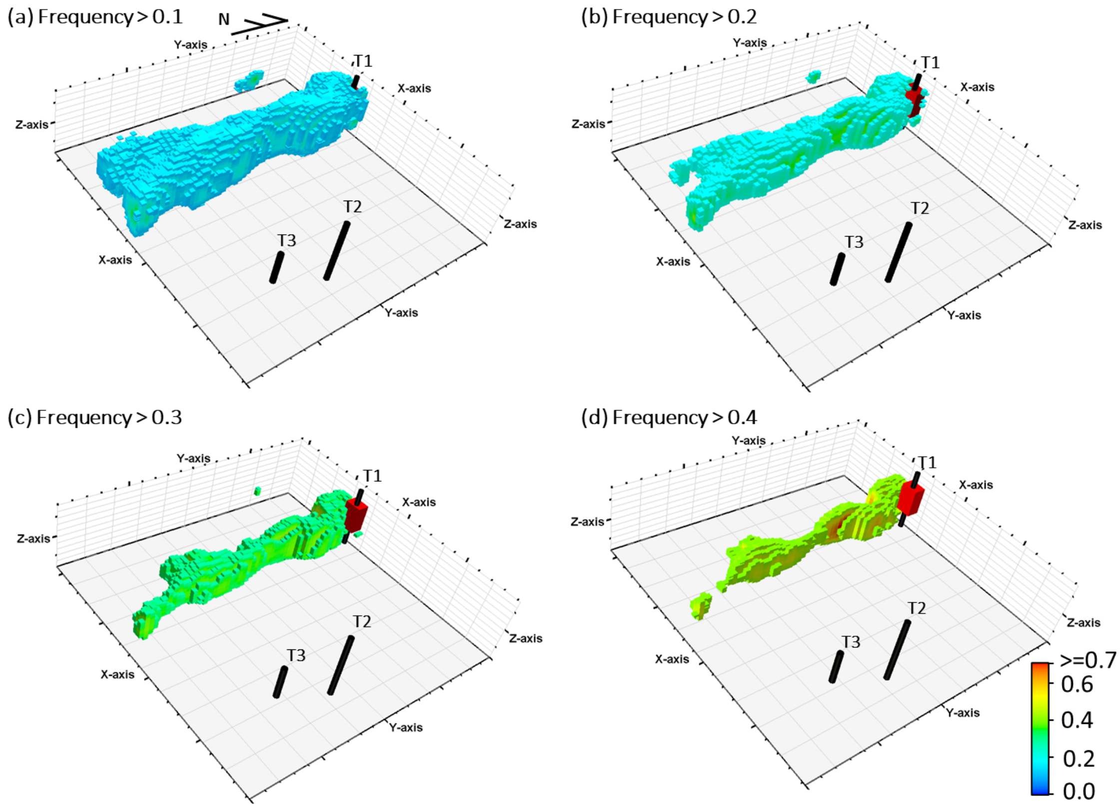

Figure 23 Filtered frequency maps based on thresholds of 0.1, 0.2, 0.3, and 0.4.

The probability map obtained from seismic data involves uncertainty, which may come from the collection and processing of seismic data itself, the non-uniqueness of the relationship between seismic attribute and cave probability, error in the interpretation of well data, etc. Thus, in practice, we may not trust the seismic probability map completely. Given a relative trust level (t), varying from 0 to 1, here a compromised probability map p_t is defined to only contain t portion of the original seismic probability map information:

$$p_t(x) = tp(x) + (1 - t)p_{prior}(x), \tag{3}$$

where x represents each cell of the geological model, $p_t(x)$ is the compromised probability map at trust level of t, $p(x)$ represents the original seismic probability map, and $p_{prior}(x)$ is the cave prior probability map prior to seismic survey. This prior probability map may come from geologic reasoning or well data interpretation. When changing the trust level from 1 to 0, the compromised probability linearly shifts from the complete seismic probability map to the complete prior probability map where no information about seismic data or its consequent probability map is kept.

In this case, we use the cave proportion interpreted from the three wells, 0.133, as the prior cave probability for each cell, i.e., $p_{prior}(x)$ = 0.133. Then we decrease the trust level from 1 to 0 (trust level = 0.7, 0.5, 0.2, and 0), and use the calculated compromised probability map at these levels and the well data for uncertainty geomodelling of caves, as shown in Figure 24. The case with trust level as 1 is just as discussed earlier in Figure 20, Figure 21, and Figure 22. It is clear that as the trust level decreases to 0, the influence of the seismic probability map on the generated cave realizations and the calculated frequency map also decreases to 0, while the variability of the generated realizations gradually increases as is shown by the frequency maps (especially the vertical sections marked by red lines) of Figure 24. Note that all these generated realizations are realistic and are conditioned to the input well data with 100% accuracy.

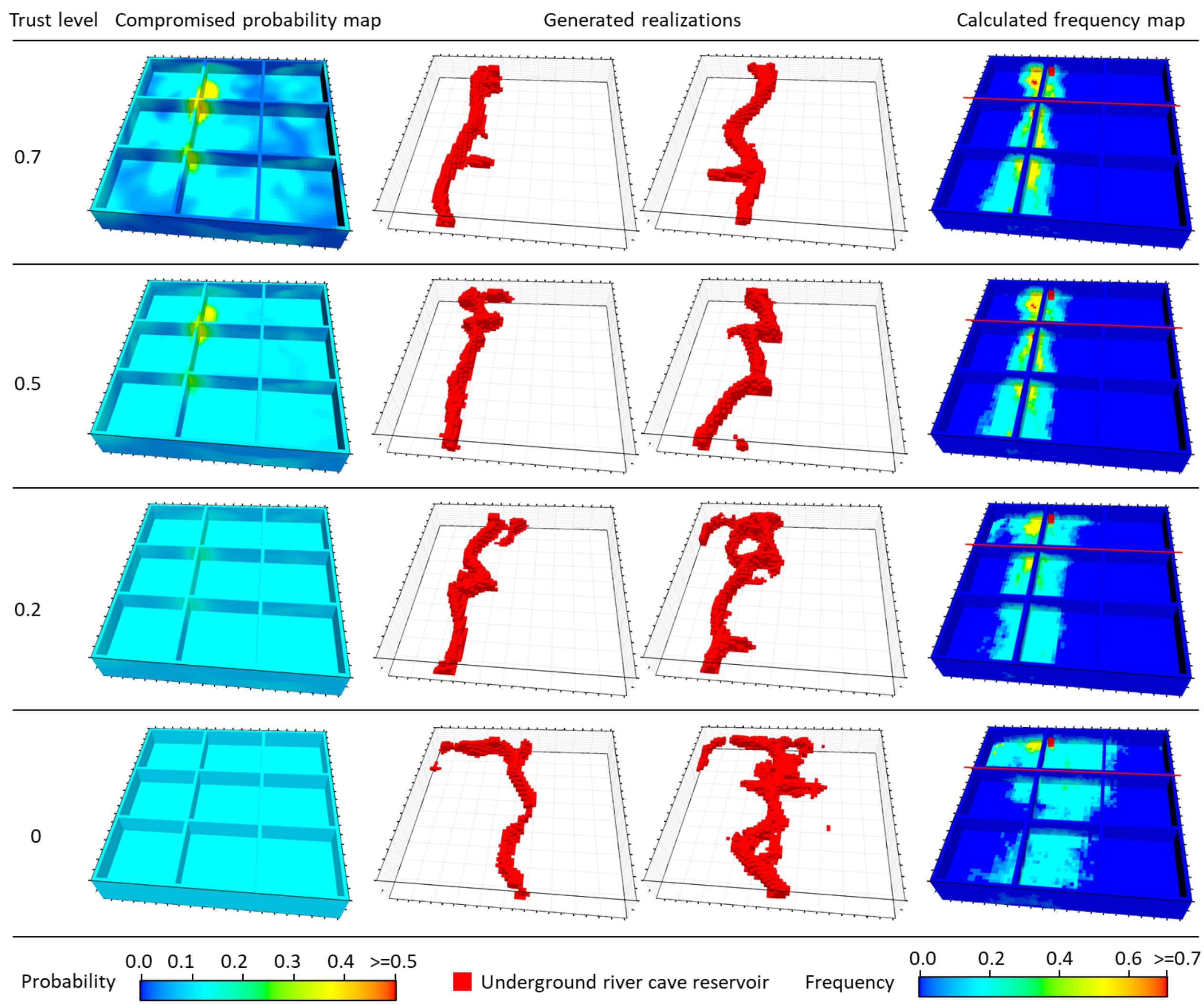

Figure 24 Compromised probability maps, generated realizations, and calculated frequency maps at various trust levels of the seismic probability map (i.e., 0.7, 0.5, 0.2, 0).

6.2 Field case 2 based on 336×256×96 cells

As described in Section 2.1, the generator trained on dataset of small size can be used for geomodelling of reservoirs with large arbitrary sizes by expanding the sizes of all inputs proportionally. Thus, here in case 2 we choose a field area of 4.2km×3.2km, with 11 wells, from Tahe cave reservoir. From well logs, 7 underground river karst cave intervals are recognized. The 3D probability map of underground river cave is calculated from seismic data with the same method as in the previous case, i.e., by combining the seismic frequency energy attribute and the relationship between the attribute and cave occurrence probability obtained from the statistics of wells. Analyses of the well data and the probability map suggests that the underground river cave of this area should be distributed between 60m to 156m beneath the paleo-geographic surface. Thus, the geo-space inside this zone is divided into 336 × 256 × 96 cells, with each cell representing 12.5m (length) × 12.5m (width) × 1m (height) which is the same as the training/test dataset. Figure 25 shows the probability map of karst cave and the distribution of well facies data in this 336×256×96-cell geo-space.

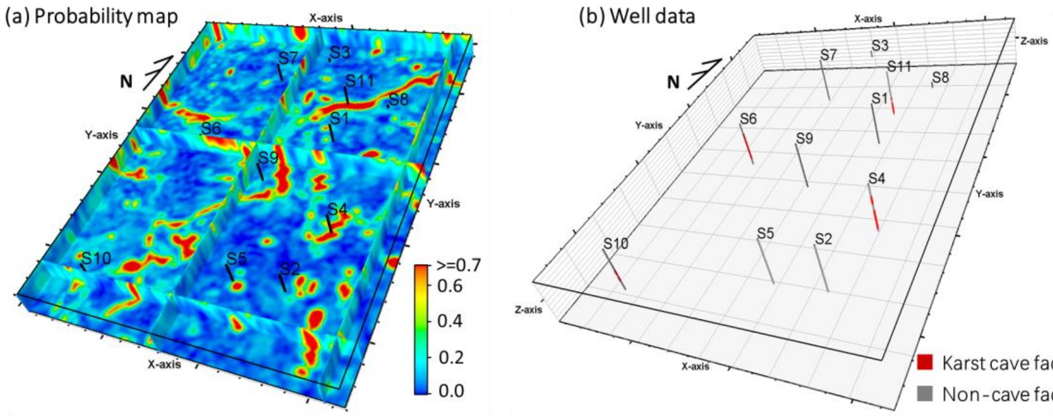

Figure 25 3D probability map of underground river karst cave and the distribution of well facies data in the study area. There are 336×256×96 cells, with each cell representing 12.5m (length) × 12.5m (width) × 1m (height).

As illustrated earlier, the pretrained generator can produce facies models of any size that is 16 times of the input latent cube size. We take the 3D probability map (with size of 336×256×96), the well data (with size of 336×256×96), and 200 groups of random latent cubes (each group has 8 channels of random latent cubes with size of 21×16×6) into the pretrained generator to produce 200 karst cave facies model realizations with 336×256×96 cells. Each realization takes 0.988 seconds on average at 1 GPU (V100).

Figure 26 (a) shows one random realization. There are a small number of localized discrete caves with very small volume and without an apparent ribbon-like pattern in the realizations. As shown in Figure 27, most of these discrete localized features are not located at the local highs of the input probability map, thus proving the occurrence of this noise may not relate to the input probability map. One possible reason is that the generator is originally trained to produce 64×64×64-size facies models from 4×4×4-size latent cubes containing Gaussian random variables and one layer of zeros outside each latent cube for zero padding, but when the generator is applied here for 336×256×96-size facies model production, each 64×64×64-size patch of the generated facies model is calculated from 4×4×4-size latent cube patches (inside the input 21×16×6-size latent cubes) and one layer of Gaussian variables outside the latent cube patches for padding. Such a small change in the padding number may result in these small, localized noises in the generated facies models.

The volumes of these cave noises are generally smaller than 2000 cells (312,500m^3). We remove these cave noises less than 2000 cells in post-processing. Figure 26 (b) shows the cleaned version of the realization in Figure 26 (a) after the post-processing removal of cave noise. The colors represent different simulated caves ordered by cave volume. Figure 26 (c) – (f) show the clean version of four other realizations.

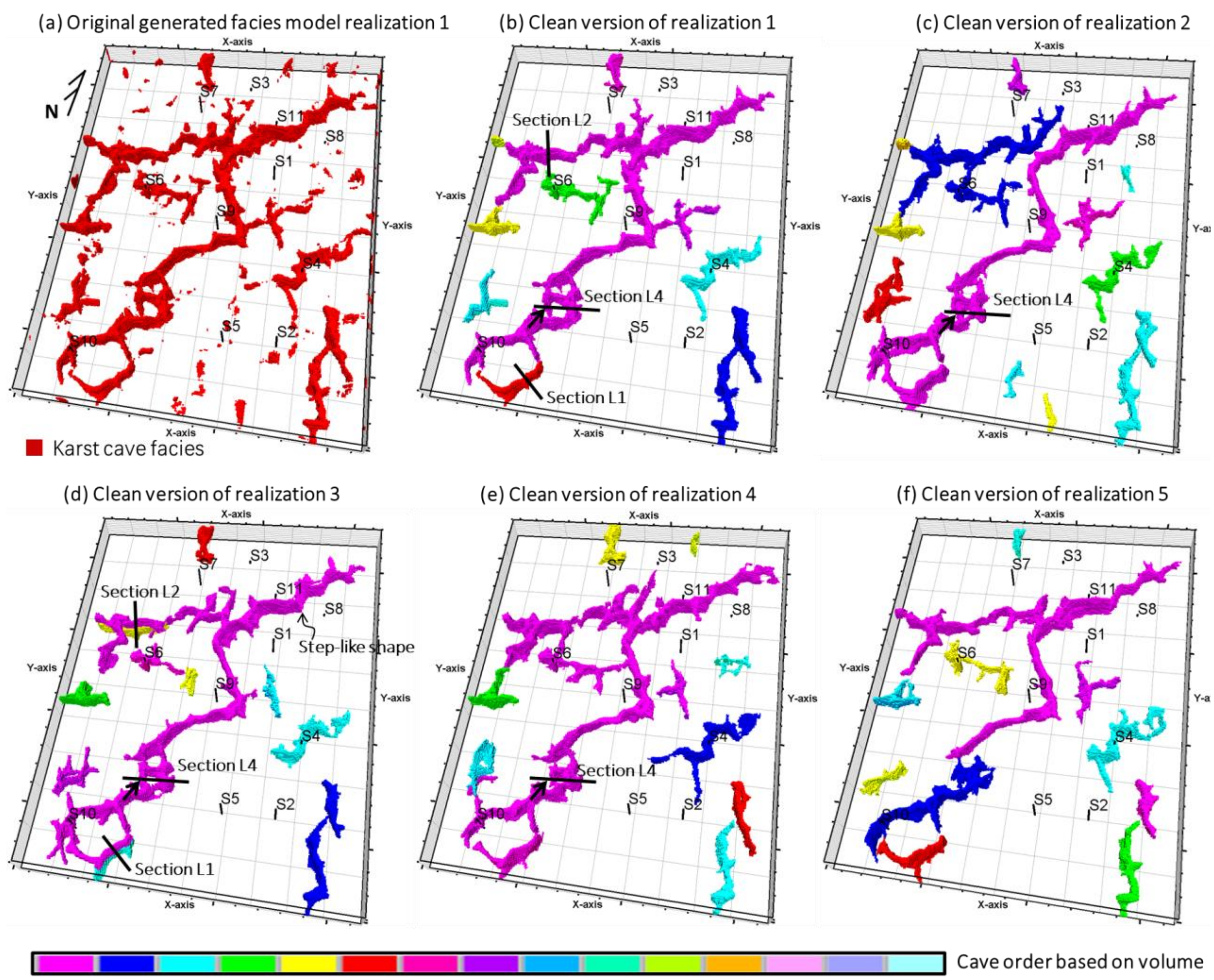

Figure 26 Original (a) and post-processed clean version ((b) – (f)) of random realizations of underground river cave reservoir for the study area. Each realization has 336×256×96 cells, with each cell representing 12.5m (length) × 12.5m (width) × 1m (height). Only underground river cave facies are shown. The color represents the order of cave based on its volume.

(a) Planar section at 62m beneath the paleo-geographic surface

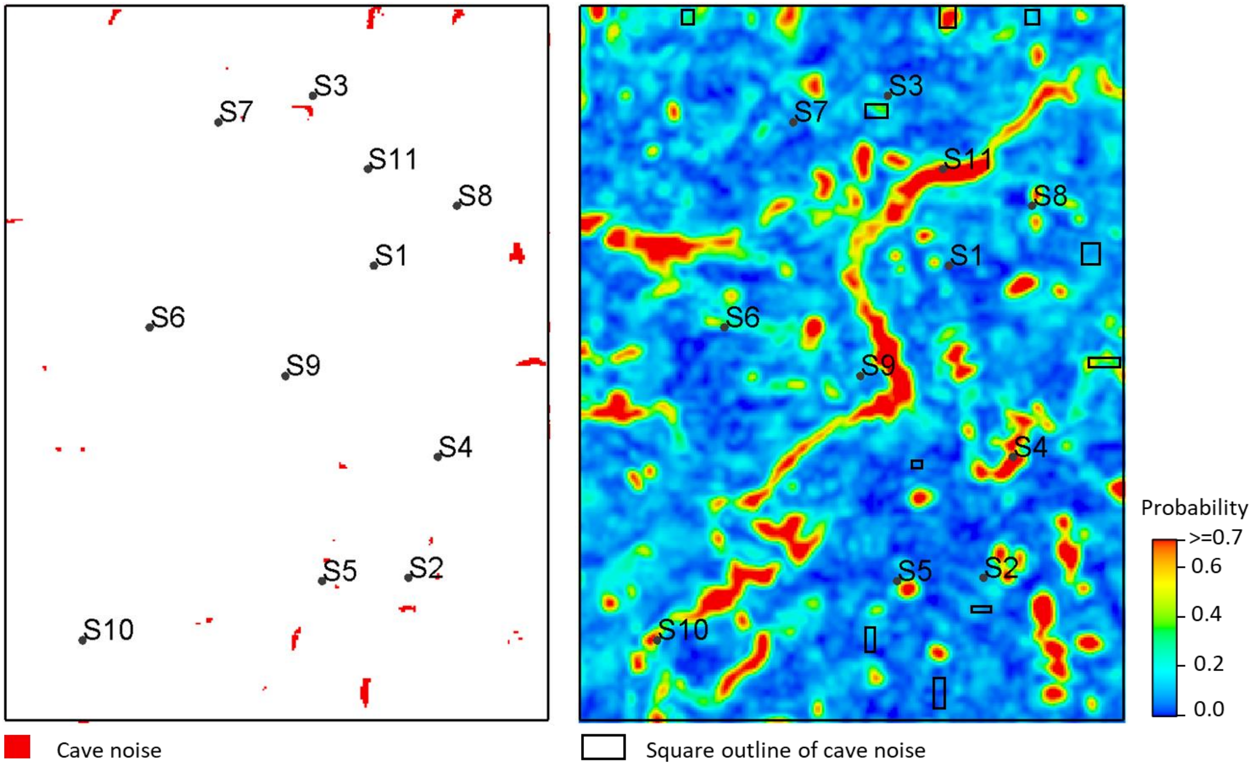

(b) Planar section at 81m beneath the paleo-geographic surface

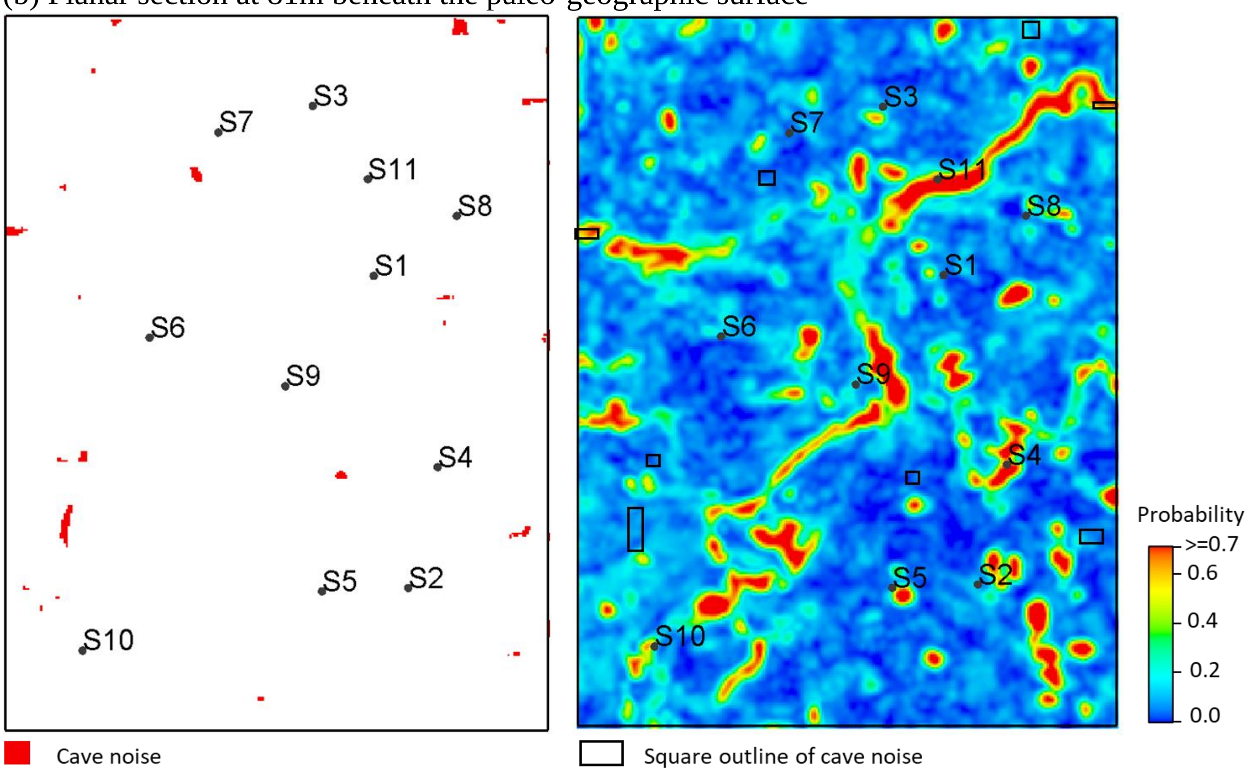

Figure 27 Cave noises (Left) of realization 1 in Figure 26 and the corresponding input probability map (Right) at different planar sections (62m and 81m beneath the paleo-geographic

surface). The large ribbon-like caves are not shown here. The outlines of these cave noises are overlain with the probability map.

The simulated caves in these realizations are consistent with the expected geological patterns, such as step-like cave shape (Figure 26 (d)), cave conduits with strikes of NNE, NNW, and nearly EW, sparse hall caves, etc. Especially, vertically-stacked double cave layers are simulated in some realizations, e.g., Figure 26 (d), at sections L1 and L2. Double cave layer feature does not exist in the training data yet it is common and important in the actual field. As is illustrated in Figure 28, double cave layers are simulated mainly because the high-value area of input probability map is large enough to accommodate double cave layers stacking vertically. Of course, one vertically large cave may also be simulated to replace double cave layers as shown in sections L1 and L2 in Figure 26 (b) and the black dashed lines in Figure 28. The simulated karst caves are also diverse. Note the various shapes of the largest pink karst cave in Figure 26. Figure 28 also illustrates a variety of shape and location of the simulated caves: a large anomaly of high probability can give either one large cave or two vertically stacked smaller caves.

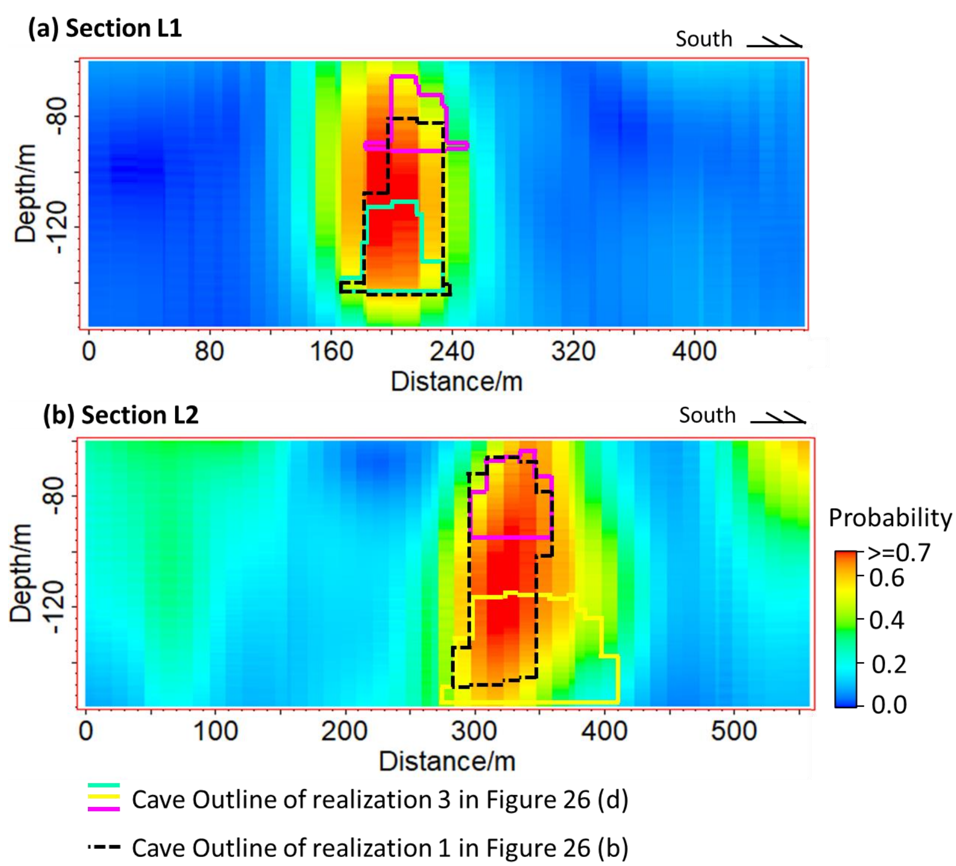

Figure 28 Outlines of simulated caves overlap with the input probability map in two vertical sections L1 and L2. The caves are from simulated realization 1 and 3 in Figure 26 (b) and (d). The two sections are marked in the two subfigures.

Like the previous case, the shape and distribution of the simulated caves are consistent with the input probability map. We use the 200 simulated realizations before post-processing removal of cave noise to calculate a frequency map of karst caves. Figure 29 shows this frequency map filtered with various thresholds (i.e., 0.1, 0.2, 0.3, 0.4, 0.5, 0.6, 0.7, and 0.8). In Figure 30 and Figure 31, we compare the input probability map with the calculated frequency map at various horizontal and vertical sections. Most high-value areas of the frequency map are distributed inside high-value areas of the probability map, although some high frequency values are distributed at low probability value areas (e.g., section 4 and section 5 in Figure 30 and Figure 31). This is mainly because, the pretrained generator uses the learned geological pattern knowledge to connect several discrete high probability anomalies to form one connected underground river cave. The occurrence of the west cave of section L4 in Figure 26 (pointed by black arrows) is just this case. Additionally, many localized high-value anomalies of the input probability map correspond to zero value in the frequency map, such as the northwest corner in the planar section of Figure 30 and the west half of section L5 in Figure 31. These anomalies are essentially noises. The pretrained generator suppresses these noises using its learned geological pattern knowledge (e.g., the underground river cave should have ribbon-like shape). The well reproduction accuracy is 100% for both cave and non-cave facies types.

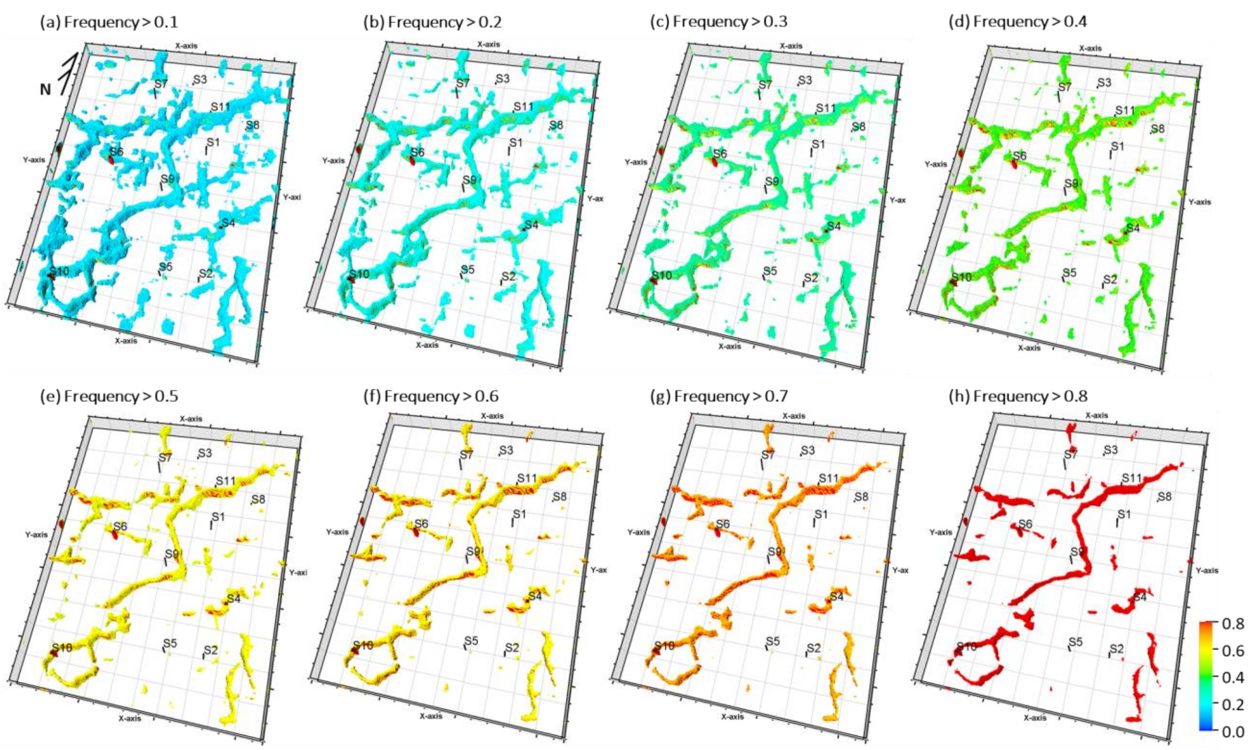

Figure 29 Karst cave frequency map of simulated caves filtered with thresholds of 0.1, 0.2, 0.3, 0.4, 0.5, 0.6, 0.7, and 0.8.

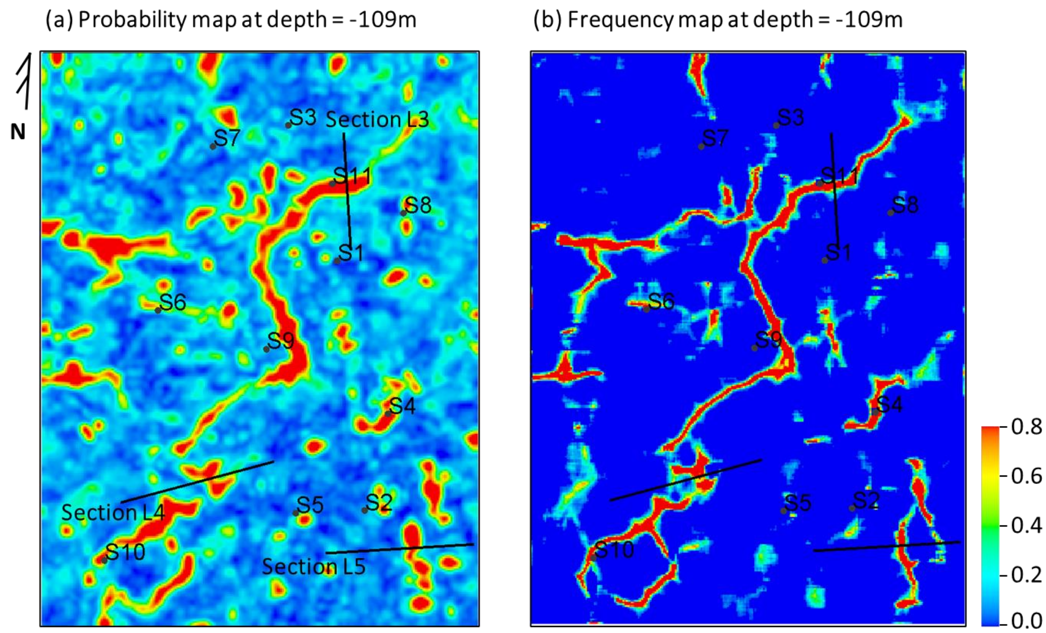

Figure 30 Comparison of the input probability map and the calculated frequency map at a horizontal section 109m beneath the paleo-geographic surface.

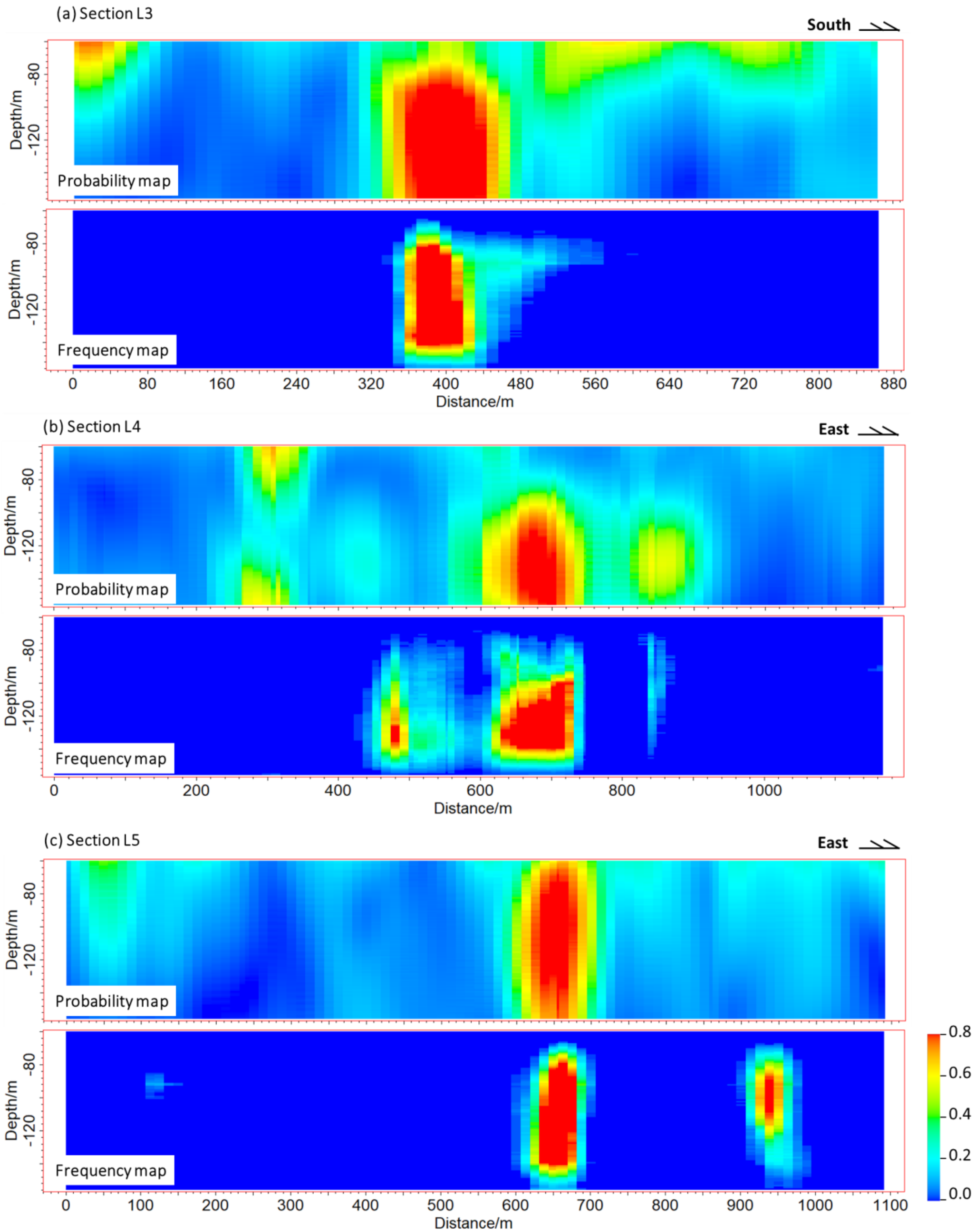

Figure 31 Comparison of the input probability map and the calculated frequency map at various vertical sections. These sections are marked in Figure 30.

The fractures (may include some faults) of this study area are recognized from seismic data via ant tracking technique used by the commercial software Petrel. Uncertainty exists in these abstracted fractures, meaning that some of them are inaccurate, and some are not recognized. In Figure 32, the fractures are overlain with the calculated frequency map of underground river cave filtered with a threshold of 0.1. We can find most parts of the filtered frequency map coincide with the distribution of fractures, such as the areas pointed out by the red arrows in Figure 32. Figure 33 shows the relationship between the percentage of the visible cells in Figure 32 and the distance to fractures, indicating apparent inclination of generated caves to develop at the vicinity of fractures. Note there is a close genetic relationship between actual underground river caves and fractures as is discussed in Section 3.1. Thus, the overlap in Figure 32 also proves the accuracy of the simulated karst caves.

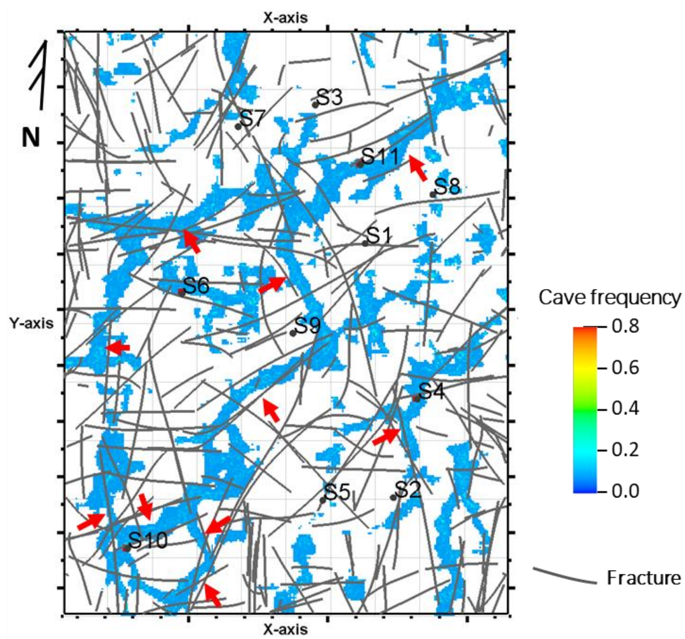

Figure 32 Fractures obtained from interpreted seismic data using ant-tracking technique, overlain with the frequency map of underground river karst cave filtered with a threshold of 0.1 for this study area. The red arrows point to the areas where the frequency map coincides with the fractures.

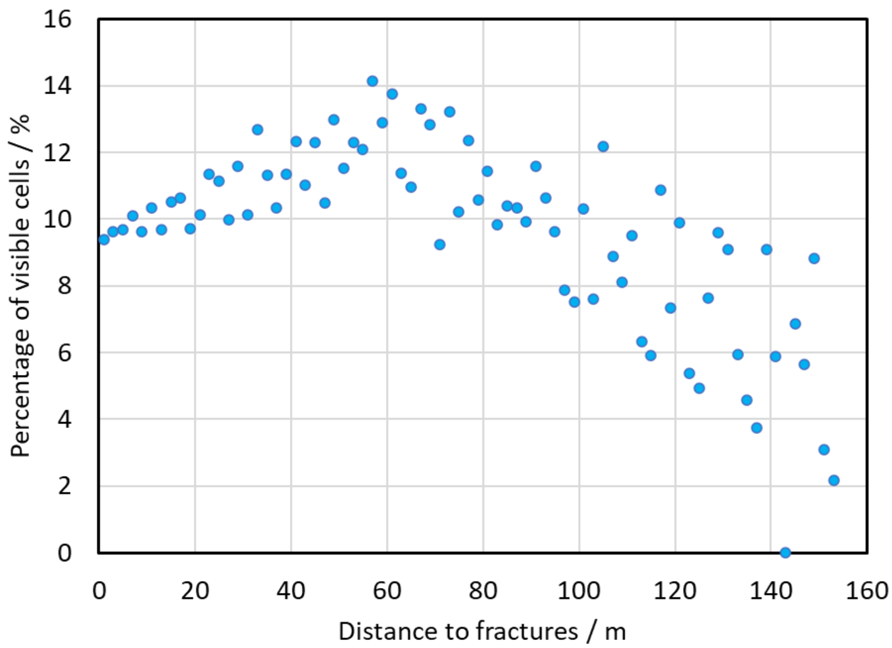

Figure 33 Relationship between the percentage of the visible cells in Figure 32 (frequency map values larger than 0.1) and the distance to fractures.

Similar to the previous case, given decreasing trust levels for the probability map as 0.7, 0.3, and 0, we calculate the compromised probability maps at the three trust levels with Equation (3). The cave proportion interpreted from wells, 0.191, is used as the prior-seismic cave probability for each cell (i.e., $p_{prior}(x)$ = 0.191). Then the compromised probability maps and the original well data are used for uncertainty geomodelling. Figure 34 shows the compromised probability maps, simulated realizations, and the corresponding cave frequency maps for the three trust levels. As the trust level decreases, the original seismic probability map has less and less influence on the generated cave realizations and until no influence when the trust level equals 0. At the same time, the realizations become more and more various and finally completely consistent with the prior probability map (i.e., 0.191 for all cells) when the trust level equals 0. All generated realizations are realistic and conditioned to the input well data with 100% accuracy.

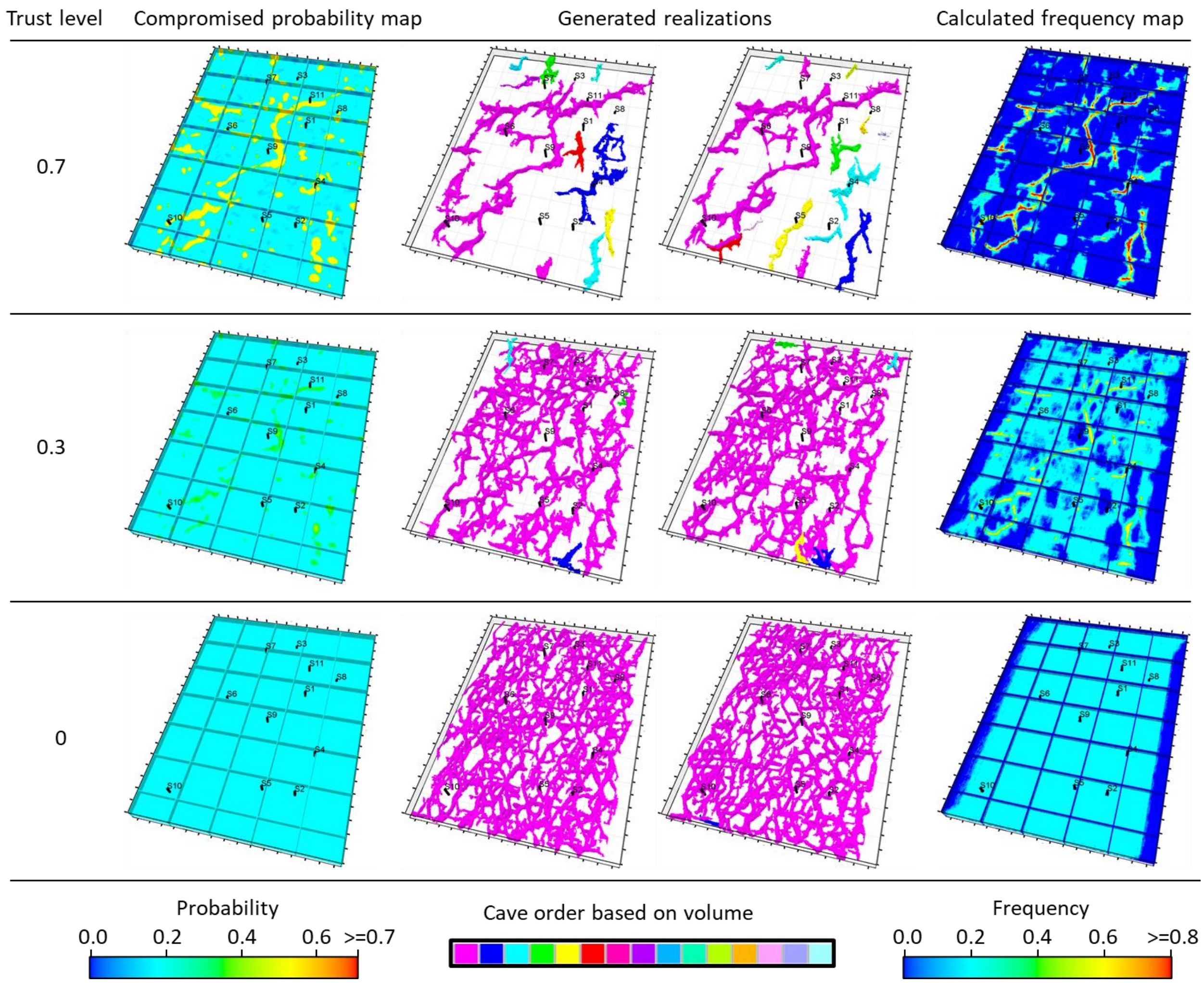

Figure 34 Compromised probability maps, consequent generated realizations, and calculated frequency maps at various trust levels for the original seismic probability map (i.e., 0.7, 0.3, and 0).

We also tried geomodelling with fewer conditioning wells. As Figure 35 (a) shows, the interpretation data of 3 wells (well S1, S4, and S6) are removed from the original input well data. Among the three removed wells, well S4 and S6 drill through underground river caves (see Figure 25). The new well data and the original seismic probability map are taken into the pretrained generator to produce 400 cave realizations. Figure 35 shows two random realizations and the cave frequency map calculated from these realizations, where the three removed wells are also shown. We can see from the generated realizations and the frequency map that, although the cave interpretation data of S4 is not taken as input, caves are produced at S4 in all realizations – with 100% cave frequency value at S4. This is due to the very strong conditioning effect of the input seismic probability map at the location of S4. For the location of well S6, the input seismic probability map has a rather weak conditioning (see Figure 25, Figure 27, and Figure 30), so no cave is produced at this location (Figure 35). Note that caves are produced at the location of S6 in all realizations when the interpretation data of S6 is used as input (Figure 26 and Figure 29). Thus, as expected, well data improves the accuracy of the simulated earth models.

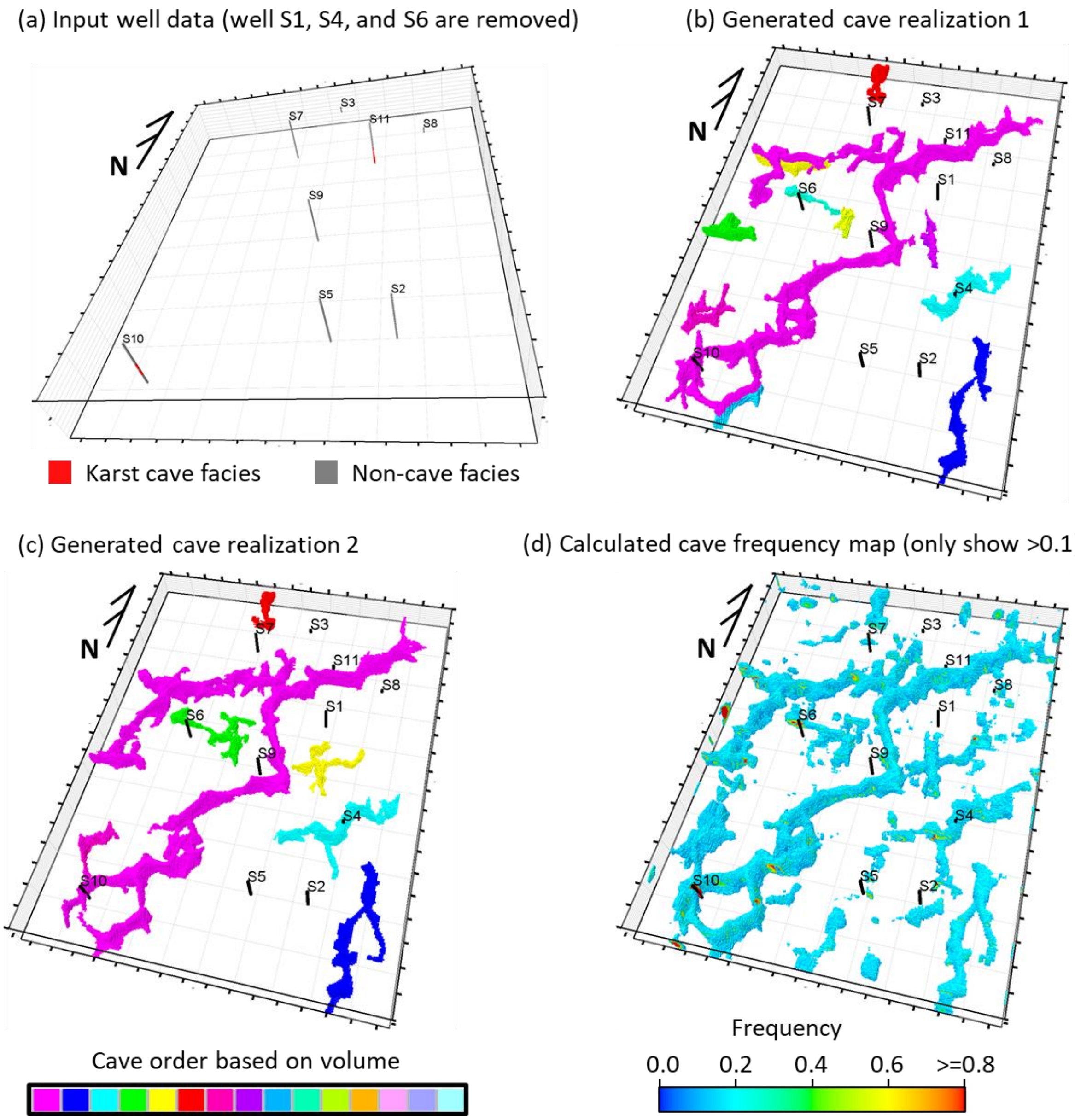

Figure 35 New input well data after removal of the interpretation data of three wells (S1, S4, and S6), two random generated cave realizations, and the calculated cave frequency map filtered by the threshold of 0.1. The three removed wells are visualized in the realizations and the frequency map.

The above analyses shows that the generator trained at 64×64×64 cells can be used to quickly produce various facies model realizations of any size, conditioned to probability map resulting from geophysical interpretation and well data. These realizations are consistent with both the geological pattern and the input conditioning data. The local noises in the input probability map are suppressed. Double cave layers are simulated in some realizations though such a feature does not exist in the training data yet is common in the field, indicating a strong generalization ability of the pretrained generator. Thus, the generator can be used for quick and accurate conditional geomodelling and uncertainty assessment in other areas of Tahe cave reservoir or other reservoirs with similar geological patterns. Given the uncertainty of the seismic probability map itself, different trust levels for the probability map can be considered when geomodelling.

7. Conclusions

This study proposes a 3D framework, GANSim-3D, for conditional geomodelling of arbitrary sizes, based on Generative Adversarial Networks (GANs). The generator of GANSim-3D only includes 3D convolutional layers, takes various 3D conditioning data and 3D random latent cubes containing random numbers as inputs, and produces a 3D facies model. The conditioning data can include sparse well facies data, low-resolution probability maps resulting from geophysical interpretation, and global features like facies proportion, channel width, etc. The original adversarial GANs loss augmented by condition-based loss is used to progressively train the generator to learn geological patterns and relationships between conditioning data and facies models. After training, when we fix the input conditioning data and randomly change the input latent cubes, multiple realistic and conditional 3D facies model realizations are produced. The trained generator can be used for geomodelling of reservoirs of large arbitrary sizes by expanding the sizes of all inputs proportionally.

A field karst cave (underground river cave) reservoir in Tahe area of China is used as an example to illustrate how GANSim-3D is used and test its field performances. We take well facies and probability map resulting from geophysical interpretations as conditioning data. First, 642 large 3D conceptual models of Tahe cave reservoir are constructed using a newly proposed process-mimicking simulation approach with parameters obtained from the field reservoir. These conceptual models are unconditional and capture the geological patterns of Tahe cave reservoirs. We crop these large-size conceptual models to build smaller-size 3D training facies models which are then used to build 3D well facies and 3D probability maps as part of the training data. Next, the generator and discriminator are trained for 40 hours, using 4 GPUs (NVIDIA Tesla V100-PCIE-32GB), 20 CPUs, and 160G RAM in parallel. The trained generator is evaluated in two synthetic cases with various metrics, showing excellent performances in producing realistic, accurate, diverse, and conditional 3D facies models. Then, we use the generator for uncertainty geomodelling of two 3D Tahe cave reservoirs of sizes 800m × 800m × 64m (divided into 64×64×64 cells) and 4200m×3200m×96m (divided into 336×256×96 cells). In both cases, multiple 3D realizations are quickly produced, being diverse and consistent with expected geological patterns of Tahe cave reservoir and the input field conditioning data (3D well data and 3D probability maps). Additionally, it turns out that the generator can automatically suppress localized noise patterns of the input probability map. Double cave layers are produced in the second field case, which do not exist in the training facies models yet are common and important in practice, indicating the robust generalization ability of the generator. Finally, various trust levels for the probability map obtained from geophysical data are also considered when geomodelling. Geomodelling with the trained generator is quite fast: each realization with 336×256×96 cells takes 0.988 seconds using 1 GPU (V100). The trained generator can be used for uncertainty geomodelling of other areas of Tahe cave reservoir or other field reservoirs with similar geological patterns.

Acknowledgments

This work was supported by the National Natural Science Foundation of China (42072146). We acknowledge the sponsors of the Stanford Center for Earth Resources Forecasting (SCERF) and support from Prof. Steve Graham, the Dean of the Stanford School of Earth, Energy and Environmental Sciences. Some of the computing for this project was performed on the Sherlock cluster at Stanford University. We would like to thank Stanford University and the Stanford Research Computing Center for providing computational resources and support that contributed to these research results.

References

Audra, P., D'Antoni-Nobecourt, J. C., & Bigot, J. Y. (2010). Hypogenic caves in France. Speleogenesis and morphology of the cave systems. *Bulletin de La Societe Geologique de France*, *181*(4), 327–335. https://doi.org/10.2113/gssgfbull.181.4.327

Berens, P. (2009). CircStat: A MATLAB toolbox for circular statistics. *Journal of Statistical Software*, *31*(10), 1–21. https://doi.org/10.18637/jss.v031.i10

Billi, A., Valle, A., Brilli, M., Faccenna, C., & Funiciello, R. (2007). Fracture-controlled fluid circulation and dissolutional weathering in sinkhole-prone carbonate rocks from central Italy. *Journal of Structural Geology*, *29*(3), 385–395. https://doi.org/10.1016/j.jsg.2006.09.008

Boersma, Q., Prabhakaran, R., Bezerra, F. H., & Bertotti, G. (2019). Linking natural fractures to karst cave development: A case study combining drone imagery, a natural cave network and numerical modelling. *Petroleum Geoscience*, *25*(4), 454–469. https://doi.org/10.1144/petgeo2018-151

Burt, P. J., & Adelson, E. H. (1987). Readings in computer vision: issues, problems, principles, and paradigms. In M. A. Fischler & O. Firschein (Eds.) (pp. 671–679). San Francisco, CA, USA: Morgan Kaufmann Publishers Inc. Retrieved from http://dl.acm.org/citation.cfm?id=33517.33571

Chan, S., & Elsheikh, A. H. (2017). Parametrization and generation of geological models with generative adversarial networks. *ArXiv Preprint*, arXiv: 1708.01810.

Chan, S., & Elsheikh, A. H. (2019). Parametric generation of conditional geological realizations using generative neural networks. *Computational Geosciences*, *23*(5), 925–952. https://doi.org/10.1007/s10596-019-09850-7

Dupont, E., Zhang, T., Tilke, P., Liang, L., & Bailey, W. (2018). Generating realistic geology conditioned on physical measurements with Generative Adversarial Networks. In *Stat* (pp. 8–16).

Feng, J., Ren, Q., & Xu, K. (2018). Quantitative prediction of fracture distribution using geomechanical method within Kuqa Depression, Tarim Basin, NW China. *Journal of Petroleum Science and Engineering*, *162*, 22–34. https://doi.org/10.1016/j.petrol.2017.12.006

Fisher, N. I. (1993). *Statistical analysis of circular data*. Cambridge: Cambridge University

Press. https://doi.org/10.1017/cbo9780511564345

Goodfellow, I., Pouget-Abadie, J., Mirza, M., Xu, B., Warde-Farley, D., Ozair, S., et al. (2014). Generative Adversarial Networks. In *Advances in Neural Information Processing Systems 27* (pp. 10–23). https://doi.org/10.1001/jamainternmed.2016.8245

Gulrajani, I., Ahmed, F., Arjovsky, M., Dumoulin, V., & Courville, A. (2017). Improved training of Wasserstein GANs. In *In Proceedings of the 31st International Conference on Neural Information Processing Systems* (pp. 5769–5779).

Jetchev, N., Bergmann, U., & Vollgraf, R. (2016). Texture synthesis with spatial Generative Adversarial Networks. In *Workshop on Adversarial Training, NIPS 2016, Barcelona, Spain* (Vol. abs/1611.0). Retrieved from http://arxiv.org/abs/1611.08207

Karras, T., Aila, T., Laine, S., & Lehtinen, J. (2017). Progressive growing of GANs for improved quality, stability, and variation. *ArXiv Preprint*, arXiv: 1710.10196.

Kingma, D., & Ba, J. (2014). Adam: a method for stochastic optimization. *ArXiv Preprint*, arXiv:1412.6980. https://doi.org/10.1109/ICCE.2017.7889386

Klimchouk, A. (2009). Morphogenesis of hypogenic caves. *Geomorphology*, *106*(1), 100–117. https://doi.org/10.1016/j.geomorph.2008.09.013

Klimchouk, A., Auler, A. S., Bezerra, F. H. R., Cazarin, C. L., Balsamo, F., & Dublyansky, Y. (2016). Hypogenic origin, geologic controls and functional organization of a giant cave system in Precambrian carbonates, Brazil. *Geomorphology*, *253*, 385–405. https://doi.org/10.1016/j.geomorph.2015.11.002

Laloy, E., Hérault, R., Jacques, D., & Linde, N. (2018). Training-image based geostatistical inversion using a spatial Generative Adversarial Neural Network. *Water Resources Research*, *54*(1), 381–406. https://doi.org/10.1002/2017WR022148

Li, S., Kang, Z., Feng, X. T., Pan, Z., Huang, X., & Zhang, D. (2020). Three-dimensional hydrochemical model for dissolutional growth of fractures in karst aquifers. *Water Resources Research*, *56*(3). https://doi.org/10.1029/2019WR025631

Li, Y., Hou, J., & Ma, X. (2016a). Data integration in characterizing a fracture-cavity reservoir, Tahe oilfield, Tarim basin, China. *Arabian Journal of Geosciences*, *9*(8), 1–12. https://doi.org/10.1007/s12517-016-2562-z

Li, Y., Hou, J., & Li, Y. (2016b). Features and hierarchical modeling of carbonate fracture-cavity reservoirs. *Petroleum Exploration and Development*, *43*(4), 600–606. https://doi.org/10.11698/PED.2016.04.12

Liu, Y., Hou, J., Hu, X., Ma, X., Zhao, B., & Qi, D. (2012). 3D modeling of paleokarst reservoir in Tahe Oilfield. *Journal of China University of Petroleum*, *36*(2), 34–44. https://doi.org/10.3969/j.issn.1673-5005.2012.02.00644

Lu, X., Zhao, M., Hu, X., & Jin, Y. (2012). Studies of 3D reservoir modeling: taking Ordovician carbonate fractured－vuggy reservoirs in Tahe Oil Field as an example. *Petroleum Geology & Experiment*, *34*(2), 193–198.

Lu, X., Wang, Y., Yang, D., & Wang, X. (2020). Characterization of paleo-karst reservoir and faulted karst reservoir in Tahe Oilfield, Tarim Basin, China. *Advances in Geo-Energy Research*, *4*(3), 339–348. https://doi.org/10.46690/ager.2020.03.11

Lucic, M., Kurach, K., Michalski, M., Gelly, S., & Bousquet, O. (2017). Are GANs created equal? A large-scale study. In *In Proceedings of the IEEE/CVF Conference on Computer Vision and Pattern Recognition* (pp. 2467–2476).

Mariethoz, G., & Caers, J. (2014). *Multiple-point geostatistics: stochastic modeling with training images*. New York: John Wiley & Sons. https://doi.org/10.1002/9781118662953

Méndez, J. N., Jin, Q., González, M., Zhang, X., Lobo, C., Boateng, C. D., & Zambrano, M. (2020). Fracture characterization and modeling of karsted carbonate reservoirs: A case study in Tahe oilfield, Tarim Basin (western China). *Marine and Petroleum Geology*, *112*, 104104–104131. https://doi.org/10.1016/j.marpetgeo.2019.104104

Mosser, L., Dubrule, O., & Blunt, M. J. (2020). Stochastic seismic waveform inversion using Generative Adversarial Networks as a geological prior. *Mathematical Geosciences*, *52*(1), 53–79. https://doi.org/10.1007/s11004-019-09832-6

Nesvold, E., & Mukerji, T. (2021). Simulation of fluvial patterns with GANs trained on a data set of satellite imagery. *Water Resources Research*, *57*(22). https://doi.org/10.1029/2019WR025787.

Pyrcz, M. J., & Deutsch, C. V. (2014). *Geoestatistical reservoir modeling*. Oxford: Oxford University Press.

Rabin, J., Peyré, G., Delon, J., & Bernot, M. (2012). Wasserstein barycenter and its application to texture mixing. In A. M. Bruckstein, B. M. ter Haar Romeny, A. M. Bronstein, & M. M. Bronstein (Eds.), *Scale Space and Variational Methods in Computer Vision* (pp. 435–446). Berlin, Heidelberg: Springer Berlin Heidelberg.

Song, S., Mukerji, T., & Hou, J. (2021a). GANSim: Conditional facies simulation using an improved progressive growing of Generative Adversarial Networks (GANs). *Mathematical Geosciences*. https://doi.org/https://doi.org/10.1007/s11004-021-09934-0

Song, S., Mukerji, T., & Hou, J. (2021b). Geological facies modeling based on progressive growing of Generative Adversarial Networks (GANs). *Computational Geosciences*. https://doi.org/https://doi.org/10.1007/s10596-021-10059-w

Song, S., Mukerji, T., & Hou, J. (2022). Bridging the gap between geophysics and geology with Generative Adversarial Networks (GANs). *IEEE Transactions on Geoscience and Remote Sensing*, *60*, 1–11. https://doi.org/10.1109/TGRS.2021.3066975

Wu, J., Zhang, C., Xue, T., Freeman, W. T., & Tenenbaum, J. B. (2016). Learning a probabilistic latent space of object shapes via 3D Generative-Adversarial modeling. In *In Proceedings of the 30th International Conference on Neural Information Processing Systems* (pp. 82–90).

Xu, X., Chen, Q., Zhang, Y., Wang, J., Li, Y., Kang, Z., et al. (2021). Research progress and prospect of Ordovician carbonate rocks in Tahe oilfield: karst feature. *Journal of Petroleum Exploration and Production Technology*, *11*(11), 3889–3902. https://doi.org/10.1007/s13202-021-01268-1

Zhang, T. F., Tilke, P., Dupont, E., Zhu, L. C., Liang, L., & Bailey, W. (2019). Generating geologically realistic 3D reservoir facies models using deep learning of sedimentary architecture with generative adversarial networks. *Petroleum Science*, *16*(3), 541–549. https://doi.org/10.1007/s12182-019-0328-4

Zheng, Q., & Zhang, D. (2021). Digital rock reconstruction with user-defined properties using conditional generative adversarial networks. *ArXiv Preprint*, arXiv: 2012.07719.

Supporting Information S1

Basics of GANs

GANs framework was initially proposed by Goodfellow (2014). It includes two neural networks called generator (G) and discriminator (D), respectively. Given many observed real samples as training dataset, the generator is designed to map a low-dimensional latent vector into a sample, while the discriminator is designed to map the generated fake or real sample into a value representing the probability of the input being real. The loss function in vanilla GANs (Goodfellow et al., 2014) is

$$L\left(G_\theta, D_\varphi\right) = \mathbb{E}_{x_r \sim p_{data}}\left[logD_\varphi(x_r)\right] + \mathbb{E}_{z \sim p_z}\left[\log\left(1 - D_\varphi\left(G_\theta(z)\right)\right)\right], \quad \text{(S1)}$$

where, L is the GANs loss, G and D are the generator and discriminator neural networks, θ and φ are trainable parameters of G and D, p_{data} is the distribution of real samples, x_r is one of the given real samples, z is input latent vector, p_z is the distribution of z, and $\mathbb{E}$ is the expectation operator. The last activation function of D is a sigmoid function. The discriminator and the generator are alternatively trained by maximizing or minimizing this loss function, respectively. Such alternative training process pushes the generator to learn the complete pattern knowledge behind the given samples. The training stops until the generator produces very realistic samples so that the discriminator cannot distinguish the fake samples from real ones. After training, the generator is kept for practical generative applications. Aside from the above loss function (Equation (S1)), several other forms of losses have also been proposed in recent years (Lucic et al., 2017), among which the Wasserstein loss with gradient penalty (Gulrajani et al., 2017) proved to have the best performances.

Traditionally, all neural network layers of the generator and the discriminator are trained concurrently, where the scale of pattern knowledge to be learned is not considered. Karras (2017) proposed progressive GANs training approach (also called the progressive growing of GANs), in which the layers of the generator and the discriminator are trained one by one to allow the pattern knowledge to be learned gradually from coarse to fine scales. Progressive training approach has proved to perform better than traditional training approach in training speed, training stability, and quality of the results.

GANs have been used for geomodelling of subsurface reservoirs with either the traditional training approach (Chan & Elsheikh, 2017, 2019; Dupont et al., 2018; Laloy et al., 2018; Mosser et al., 2020; Nesvold & Mukerji, 2021; Zhang et al., 2019) or the progressive training one (Song et al., 2021a); with whichever way, the generator learns geological patterns from given training facies models. With the learned pattern knowledge, the trained generator can thus produce facies models consistent with the learned patterns, i.e., unconditional geomodelling.

Lucic, M., Kurach, K., Michalski, M., Gelly, S., & Bousquet, O. (2017). Are GANs created equal? A large-scale study. In *In Proceedings of the IEEE/CVF Conference on Computer Vision and Pattern Recognition* (pp. 2467–2476).

Supporting Information S2

GANSim: a direct conditional simulation approach based on improved GANs

To directly achieve conditional geomodels, i.e., to get generated facies models consistent with both the expected patterns and the given conditioning data (e.g., well data), first, the generator needs to take in various conditioning data, and second, the generator needs to learn the relationship between the input conditioning data and the output facies model in addition to the geological pattern knowledge. Such a relationship is the key to achieve conditioning, and thus is called conditioning ability. Song et al. (2021b, 2022) proposed the GANSim framework to directly train such a generator, based on a progressive training method.

In GANSim, three types of conditioning data are considered: non-spatial global features of reservoirs (e.g., facies proportion and channel sinuosity), sparse well facies interpretations, and spatially distributed probability maps of all facies calculated from geophysical data. Figure S2 shows the input pipelines for the three types of conditioning data for an example of producing 2D facies models of sinuous channels. The conditioning data related to global features are concatenated with the input latent vector and go through all layers of the generator. Well facies data are first downsampled into various progressive resolutions (e.g., 8×8) and then converted into feature cubes (e.g., the feature cube with size of 8×8×16) with 1×1 convolutional layers. These feature cubes are finally concatenated with the feature cubes at the same resolution (e.g., the feature cube with size of 8×8×128) in the main pipeline of the generator. The input pipeline for probability maps is the same as that of well data.

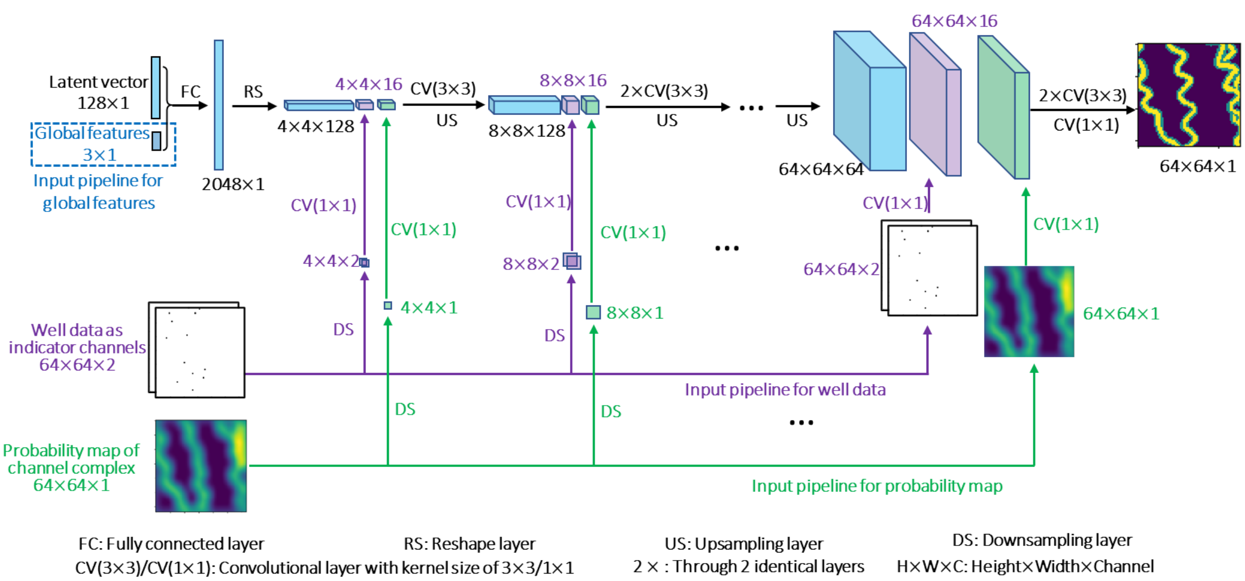

Figure S2 Input pipeline design of generator for three types of common conditioning data (non-spatial global features, sparse well facies data, and probability maps) in an example of producing 2D facies models of sinuous channels (modified from Song et al., 2022). Global features (e.g., facies proportion) are concatenated with the input latent vector; well data are first downsampled into various resolutions and then converted into feature cubes with 1×1 convolutional layers, which are further concatenated with other feature cubes of the same resolution in the main pipeline; the input pipeline design for probability maps is the same as that of well data.

To let the generator learn the conditioning ability, a specially designed loss function (called condition-based loss function) is introduced in GANSim, while the original GAN loss (Equation (S1)) is kept to guarantee the learning of geological pattern knowledge. The general form of this condition-based loss function is

$$L(G)_{con} = \mathbb{E}_{z\sim p_z, con_{in}\sim p_{con}} Dist(f_{con}[G(z, con_{in})], con_{in}). \tag{S2-1}$$

Here, con_{in} is the input condition (e.g., well facies data), p_{con} is the distribution of con_{in}, and $Dist$ is some type of distance function. f_{con} is a predefined inversion function that maps the generated facies model $G(z, con_{in})$ into the correct condition values it corresponds to. $L(G)_{con}$ essentially represents the inconsistency between the input condition con_{in} and the generated facies model ($G(z, con_{in})$). By minimizing $L(G)_{con}$, the generator is forced to learn the relationship between the input condition and the output facies model, i.e., conditioning ability.

According to the general form (Equation (S2-1)), the condition-based loss function of global features is specified as

$$L(G_\theta)_g = \mathbb{E}_{z\sim p_z, g\sim p_g} \parallel f_g[G(z,\ g)] - g \parallel_2, \tag{S2-2}$$

where, g is input (one or multiple types of) global features, p_g is the distribution of all possible g, and f_g maps generated facies models into the corresponding real global features. In some cases, f_g is hard to obtain, so an additional neural network may be trained as f_g (see Song et al., 2021b). $Dist$ in Equation (S2-1) is specified as Euclidean L2 distance here, i.e., $\parallel\cdot\parallel_2$.

The condition-based loss of well facies data is specified as

$$L(G_\theta)_w = \mathbb{E}_{z\sim p_z, w\sim p_w} \parallel I_{wloc} \odot [G(z,\ w)] - w \parallel_2, \tag{S2-3}$$

where, w is input well data, p_w is the distribution of all possible w, I_{wloc} is the indicator of well locations, and $\odot$ is the element-wise product operator.

The condition-based loss of probability map is specified as

$$L(G)_p = \mathbb{E}_{z_1, z_2, \ldots, z_m \sim p_z, p\sim p_p} \parallel f_p[G(z_1, p), G(z_2, p), \cdots, G(z_m, p)] - p \parallel_2, \tag{S2-4}$$

where, $z_1, z_2, \ldots, z_m$ are random samples of the input latent vector z from its distribution p_z, p represents input probability maps for all facies types, p_p represents the distribution of possible p, and f_p calculates the frequency map (in fraction) for each facies type from m generated facies models. Parameter m is a predefined hyperparameter. For a facies type F, the value at each location of the frequency map of this type is calculated by the sum of occurrence of that facies at that location in the m generated models divided by m:

$$f_p = \frac{\sum_{i=1}^{i=m} \mathbb{1}[G(z_i,\ p) = C(F)]}{m}. \tag{S2-5}$$

Here, $C(F)$ represents the code of facies type F, and the indicator function $\mathbb{1}(\cdot)$ equals 1 if the condition inside the bracket is satisfied, otherwise equals 0.

These three types of conditioning data are not necessarily all included depending on specific cases of observed conditioning data. The total loss is a weighted combination of the condition-based loss and the original GANs loss:

$$L(G, D)_{total} = \beta_1 L(G, D) + \beta_2 L(G)_{con}. \tag{S2-6}$$

Here, β_1 and β_2 are predefined weights. When training the generator, the two types of losses are both minimized, while only the GANs loss is maximized when training the discriminator. GANSim uses the progressive training approach. For example, in Figure S2, the first convolutional layer (and the FC layer) at the resolution of 4×4 is initially activated and trained after taking in the 4×4-conditioning well data and probability map; then, the following two convolutional layers at the resolution of 8×8 are further activated and trained together with the previous layers after taking in the 8×8-conditioning data. In this way, all successively higher-resolution layers of the generator are gradually activated and trained to learn the geological patterns and conditioning ability from coarse to fine scales. After training, the generator can produce facies models consistent with both the geological patterns and the input conditioning data. Once the input latent vector changes, multiple conditional facies model realizations are produced.

Supporting Information S3

Multi-Scale Sliced Wasserstein Distance combined with Multi-Dimensional Scaling (MS-SWD-MDS)

MS-SWD is proposed by Karras et al., (2017) to evaluate the distance in multi-scale spatial structures between two groups of data. Here we show the calculation steps of MS-SWD with an example of two groups of facies models (64×64, 2D). As Figure S3 shows, each group contains M facies models. First, the Laplacian pyramid representations (Burt & Adelson, 1987) of each facies model in both groups is calculated from resolution of 64×64 to 16×16. The Laplacian pyramid representations reveal the structures of the original facies models at different scales. Second, multiple (n) small patches (p×p pixels) are randomly extracted from the Laplacian pyramid representation of each facies model at each level, to obtain M*n patches from each group of facies models at each level. Third, these patches are normalized with respect to the mean and the standard deviation of each patch. Finally, the sliced Wasserstein distance (SWD), an efficient approximation to the Wasserstein distance (Rabin et al., 2012), between the patches from each group at each level is calculated. MS-SWD over different levels can be averaged as single value to represent the distance between two distributions.

MDS is commonly used to project high-dimensional data into 2D or 3D space to visualize their relationship, based on certain type of distance between each pair of the data. MS-SWD is originally used to calculate the distance between two large groups of data. Song et al., (2021a) proposed to combine MS-SWD with MDS (MS-SWD-MDS) to project the two groups of data into 2D space. In the method, each large group is divided into many small groups, and the MS-SWD is calculated for each pair of the small groups inside the two large groups. Then, all small groups are projected into 2D space using MDS, based on the calculated MS-SWD (average of MS-SWD) among these small groups. Each point in MDS represents one small group of data.

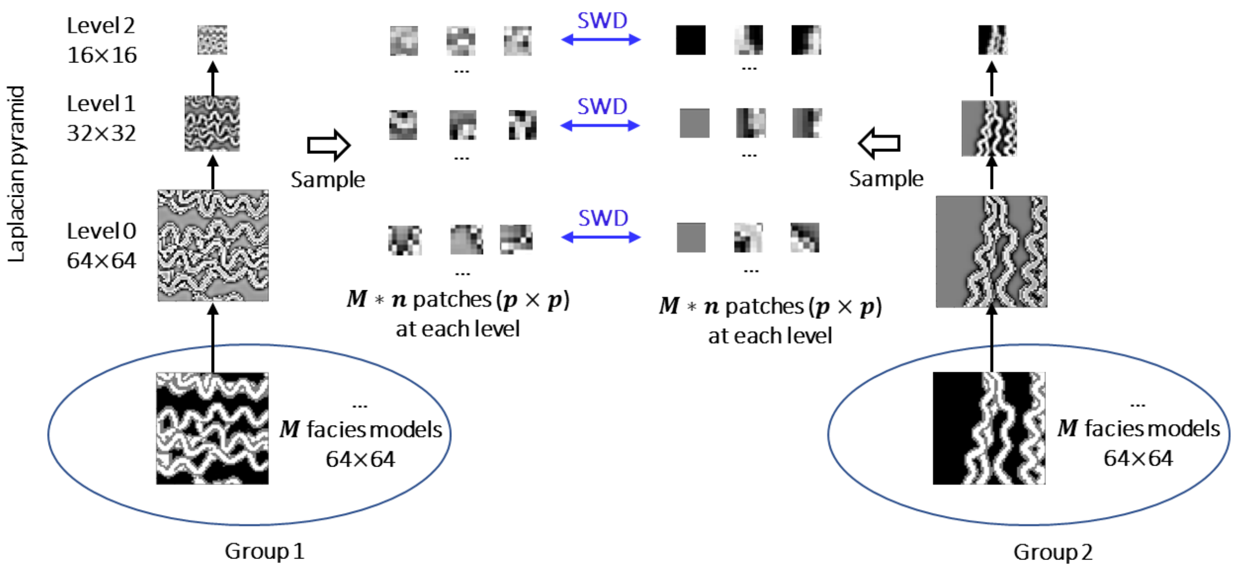

Figure S3 Schematic illustration of how MS-SWD is calculated with an example of two groups of 2-D facies models.

Burt, P. J., & Adelson, E. H. (1987). Readings in computer vision: issues, problems, principles, and paradigms. In M. A. Fischler & O. Firschein (Eds.) (pp. 671–679). San Francisco, CA, USA: Morgan Kaufmann Publishers Inc. Retrieved from http://dl.acm.org/citation.cfm?id=33517.33571

Rabin, J., Peyré, G., Delon, J., & Bernot, M. (2012). Wasserstein barycenter and its application to texture mixing. In A. M. Bruckstein, B. M. ter Haar Romeny, A. M. Bronstein, & M. M. Bronstein (Eds.), *Scale Space and Variational Methods in Computer Vision* (pp. 435–446). Berlin, Heidelberg: Springer Berlin Heidelberg.

Supporting Information S4

Brief discussions about the weights for various types of losses

Training of the GANs used in this paper involves three types of losses including the original GANs loss and the condition-based losses for well data and probability map (Equation (1)). We tried different combinations of the weights for these losses and then evaluated the performances of the trained generators in terms of the conditioning effect to input well data and probability map, diversity, and realism of the produced facies models. As shown in Figure S4, the weight for original GANs loss (β_1) is set as 1, while the weights for well data and probability map condition-based losses (β_2 and β_3) ranges from 0.0028 to 43.75 and 0.00016 to 12.5, respectively. We take the well data and probability map of the synthetic case 2 (Figure 12 (b) and (c)) into the trained generators. Figure S4 shows the produced random facies models, the frequency maps of cave facies, and the well data reproduction accuracy values for each weight combination.

We suggest to set the weight for well condition-based loss (β_2) and the weight for probability map condition-based loss (β_3) as 0.07 to 0.35 and 0.5 to 2.5, while the weight for the original GANs loss is set as 1. The weight β_2 represents a tradeoff between the conditioning of well data and the realism of the facies models produced by the trained generator, while β_3 represents a tradeoff between the diversity and the realism of the produced facies models. Note that the process of enforcing the consistency of the produced facies models with the input probability map (by using a larger β_3 value) is essentially a process of strengthening the diversity of the produced facies models.

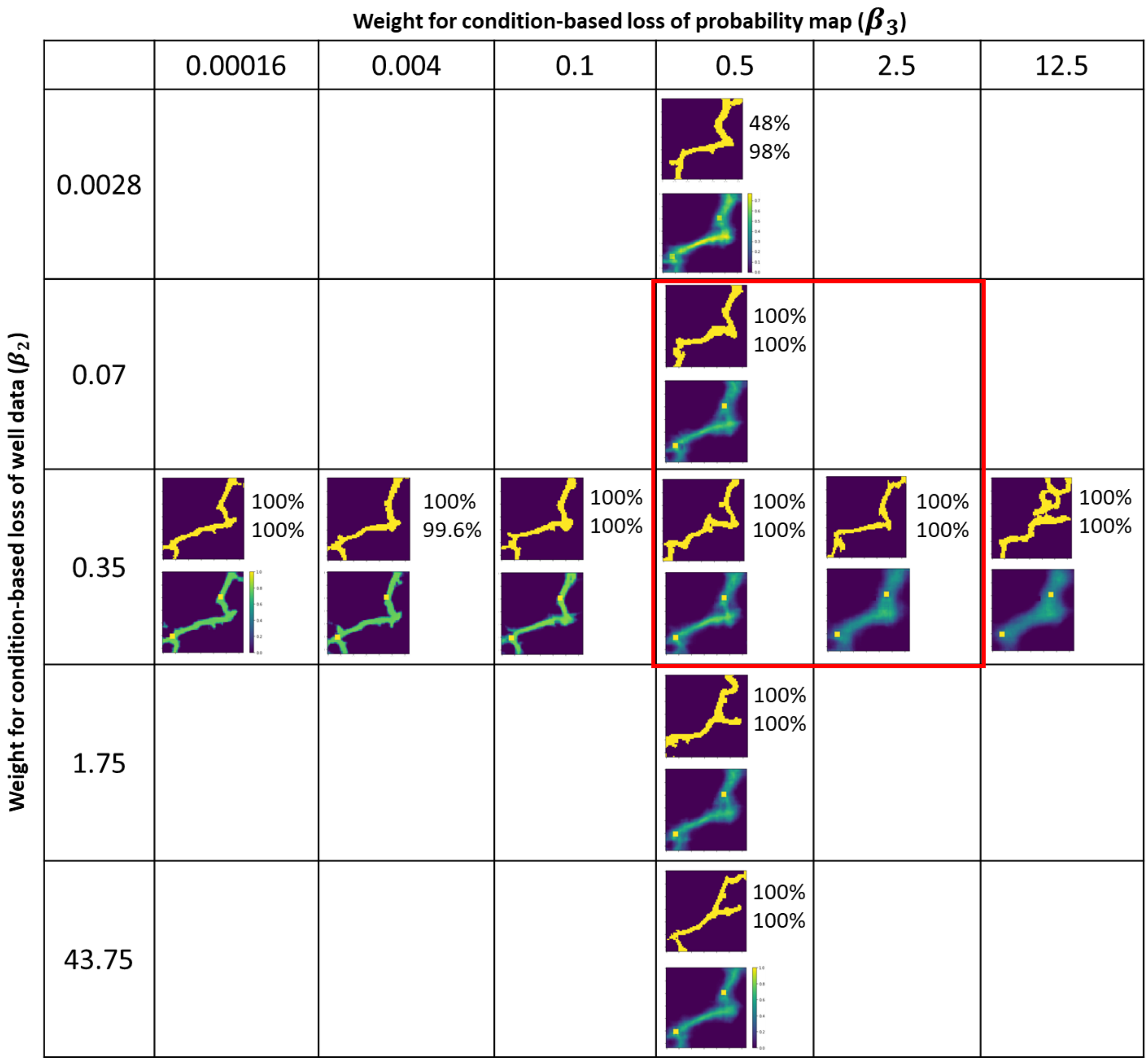

Figure S4 Horizontal sections (32nd layer of cells from top) of the produced random facies models (top) and frequency maps of cave (bottom) and well data reproduction accuracy values for cave and non-cave facies types resulting from generators trained using different weight combinations. The weight for the GANs loss is set as 1.